EFFECTS OF MECHANICAL STRESSES ON LITHIUM ION BATTERIES

by

Hyoncheol Kim

A dissertation submitted in partial fulfillment
of the requirements for the degree of
Doctor of Philosophy
(Mechanical Engineering)
in The University of Michigan
2009

Doctoral Committee:

Professor Ann Marie Sastry, Chair
Professor James R. Barber
Associate Professor Christian M. Lastoskie
Associate Professor Wei Lu

© Hyoncheol Kim 2009
All Rights Reserved

To My Parents

ACKNOWLEDGEMENTS

First of all, I would like to thank Prof. Ann Marie Sastry for her guidance and support. I was lucky to have her as my advisor because I have learned not only how to solve problems in science and technology from her great expertise, but also and more importantly how we can contribute to the world with what we can do for the better future. Her enthusiasm toward life and work is the most valuable thing I have learned at school and will always guide me throughout my life and career.

Many thanks go to my committee members, Prof. James R. Barber, Prof. Christian M. Lastoskie, and Prof. Wei Lu for serving on my committee and providing your valuable advices on my thesis.

I am very grateful to all of our current and former group members, Dr. Myounggu Park, Mr. Xiangchun Zhang, Mr. Myoungdo Chung, Mr. Min Zhu, Mr. Sangwoo Han, Mr. Dong Hoon Song, Ms. Qiuye Jin, Dr. Chia-Wei Wang, Dr. Munish V. Inamdar, Dr. Fabio Albano, Dr. Yenhung Chen, Dr. Kimberly Cook, Dr. Yun-Bo Yi, Dr. Taeyong Kim, Ms. Tahira Reid, and Mr. Peter Verhees for their support and sharing the wonderful moments for the past years.

I also would like to thank my friends, Jiwon, Chi-Shan, Jung Kap and Jong-Hoon for their help and encouragement. Most importantly, I would like to thank my parents Ip Kwon Kim and Bup Jin Song, and my sister Hyun Hee for their love and support. I also would like to thank my parents in-law, Jeong Hong Chung and Myung Sook Lee, and

finally, I would like to thank my lovely wife, Ja Won for her being with me.

Also, support for my thesis work by the U.S. Army Research Office, Dr. Bruce LaMattina, Program Monitor, is gratefully acknowledged.

TABLE OF CONTENTS

DEDICATION ii

ACKNOWLEDGEMENTS iii

LIST OF TABLES vii

LIST OF FIGURES viii

ABSTRACT x

CHAPTER

I. INTRODUCTION 1

BIBLIOGRAPHY 5

II. MULTIFUNCTIONAL COMPOSITE MATERIALS: CONSIDERATION OF LOADS IN EMBEDDED AND INTEGRATED LI BATTERIES 6

INTRODUCTION 6

METHODS 10

STRUCTURAL SIMULATIONS 10

MICRO-STRUCTURAL SIMULATIONS 15

RESULTS 20

DISCUSSION 27

CONCLUSIONS AND FUTURE WORK 28

BIBLIOGRAPHY 29

III. COUPLING EFFECTS OF MECHANICAL STRESSES AND ELECTROCHEMICAL CYCLES IN A CARBON FIBER LITHIUM ION BATTERY: EXPERIMENTAL STUDY 31

INTRODUCTION..... 31

METHODS……..... 33

MATERIALS AND BATTERY CONFIGURATION..... 33

EXPERIMENT SETUP AND MECHANICAL TESTS …..... 35

ELECTROCHEMICAL TECHNIQUES 35

RESULTS AND DISCUSSION…..... 42

CONCLUSIONS AND FUTURE WORK …..... 55

BIBLIOGRAPHY.....57

IV. MOLECULAR DYNAMICS SIMULATION OF LITHIUM ION DIFFUSION IN GRAPHITE UNDER MECHANICAL STRESSES.....59

INTRODUCTION.....59

METHODS……..... 61

POTENTIAL FUNCTIONS 61

SIMULATION AND MEASUREMENT 65

RESULTS AND DISCUSSION…..... 67

CONCLUSIONS AND FUTURE WORK …..... 70

BIBLIOGRAPHY.....74

V. CONCLUSIONS AND FUTURE WORK……..... 76

LIST OF TABLES

Table 2.1: Battery powered unmanned aero vehicle: component mass and power requirement 7

Table 2.2: Thickness and material properties of layers in WASP wing 14

Table 2.3: Thickness and material properties of layers in PowerFiber 17

Table 2.4: Material properties and simulation configurations used for micro-scale simulation 19

Table 2.5: Maximum von Mises stresses from various sources 21

Table 4.1: Parameters for Brenner Potential 64

Table 4.2: Parameters for Lennard-Jones Potential……..……..66

LIST OF FIGURES

Figure 1.1: Advances in primary battery specific energy, adapted and modified from the reference..…….....2

Figure 2.1: Structures and loads: Mechanical stresses in real world come from various sources including structural embedment, fabrication, and electrochemical reaction.…….....9

Figure 2.2: WASP (callout) plane strain beam model showing layered structure…….12

Figure 2.3: Layered structure of PowerFiber…….16

Figure 2.4: (top) Compression model of particulate electrode (bottom) maximum von Mises stress vs. volume fraction of active material…….18

Figure 2.5: Maximum von Mises stress distribution due to structural loadings in WASP wing section…….22

Figure 2.6: Maximum von Mises stress distribution due to structural loadings in PowerFiber under bending……...23

Figure 2.7: Maximum von Mises stress distribution due to structural loadings in PowerFiber under torsion..……...24

Figure 2.8: Maximum von Mises stress distribution due to thermal expansion in WASP……..25

Figure 2.9: Maximum von Mises stress distribution due to thermal expansion in PowerFiber……...26

Figure 3.1: Schematic of battery configuration and fabricated battery…….34

Figure 3.2: battery loaded in a material tester and connected to a potentiostat……..…..36

Figure 3.3: (a) load-elongation curve of battery under uni-axial tension …… 37

Figure 3.3: (b): carbon fibers are gradually aligned as the tow is stretched, but uniform strain cannot applied to individual fibers …….. 38

Figure 3.4: change in potential is measured while battery is discharged with a constantly imposed current in galvanostatic cycling. …….. 40

Figure 3.5: in cyclic voltammetry, (a) potential is controlled as a triangular function with various potential scan rates and (b) resulting current in a reversible system shows peaks in both scan directions. ……. 41

Figure 3.6: galvanostatic discharge/charge curve, (top inset) showing gentle curve due to electrolyte decomposition, (bottom inset) voltage plateau due to staging effects……..…..44

Figure 3.7: cyclic voltammogram with potential scan rates between 0.1 and 1.6 mV/s in a control sample……..……45

Figure 3.8: distinct current peaks appear when graphite is cycled with very low potential scan rate (1mV/s) ……..…… 47

Figure 3.9: cyclic voltammogram with various strains……..……48

Figure 3.10: peak current vs. square root of potential scan rate. Regression lines are added to see changes in the relationship with respect to the applied loadings …… 50

Figure 3.11: slopes from Figure 3.7 are plotted against strain. Slopes vary, but not in a significant pattern……...…..51

Figure 3.12: measured load changes as lithium ions intercalate into graphite as shown with the charge and current curves……..……53

Figure 3.13: change in measured loads is directly proportional to the amount of lithium ions inserted into graphite……54

Figure 4.1: inter atomic angle configuration among atoms i, j, and k 63

Figure 4.2: visualization of lithium intercalated graphite at stage 1…….……68

Figure 4.3: diffusion coefficient of lithium ions in graphite (left) no strain was applied to graphite (right) graphite was stretched by 1% in the perpendicular direction of graphene lattice……...….69

Figure 4.4: graphite lattice spacing during stage 1 72

Figure 4.5: stress-strain curve of graphite stretched in perpendicular direction to the graphene lattice. 73

ABSTRACT

Structural batteries are multifunctional materials that are expected to perform multiple roles, i.e. power generation and mechanical support. Properly realized, the concept can dramatically improve gravimetric properties by elimination of parasitic masses tolerated in conventional devices. However, the significant structural loads that such batteries would be expected to bear, given their multiple roles, would exceed those experienced by conventional batteries, and thus must be studied and understood in the context of device safety, lifetime and cost.

Key sources of mechanical stresses were identified and quantified in this effort, including manufacturing-induced loads, thermal loads, kinetic loads and structural loads. It was found that stresses due to compression during electrode fabrication can be as large as 2000 MPa, thus having the potential to induce mechanical failure of constituent materials, while stresses induced by structural loads in an unmanned vehicle example studied, were less than 1 MPa. Thermal stresses were found in one embodiment, to exceed 100 MPa, largely due to mechanical confinement of batteries embedded for structural support.

Supporting experiments were conceived in this work to study the effect of loads on electrochemical performance. A novel design of a structural battery was developed, to simultaneously conduct mechanical and electrochemical experiments. Diffusion coefficients were determined while various loadings were applied. Also, stresses exerted on the battery were observed while the battery was charged and discharged. Statistically

meaningful correlation was not observed for diffusion coefficients with respect to stresses, but forces applied to carbon fiber significantly varied during charging/discharging of batteries, and the magnitude of variance of force was strongly correlated with the number of charges.

Molecular dynamics simulations, finally, were performed to examine findings from experiments. Diffusion coefficients of lithium ions were measured while graphite lattices were stressed. Simulation results differed substantially from experimental findings, in that substantial alterations in diffusivities were predicted with application of load. Future work should focus on rationalizing the differences in these elements, by development of improved experiments, and improved accounting for disorder, in simulations.

CHAPTER I

INTRODUCTION

Since Alessandro Volta developed the first electric cell in 1800, batteries have multiplied their capacity through innovations in material selection and processing (Figure 1.1) [1]. The maximum capacity of a battery, however, is limited by the materials' theoretical capacity in any circumstances. Looking at this limitation out of the box, a new concept has emerged, known as a structural battery. Structural battery is a multifunctional material that can store electric energy and also function as a structural member. This type of battery is expected to have outstanding gravimetric properties such as specific energy and specific power by removing parasitic masses of canisters that were unavoidable in conventional batteries. Structural batteries can be used in applications where gravimetric properties are critical such as micro air vehicles, satellites, and portable military devices.

Despite of the promising features of a structural battery, it is of our great concern whether the stresses externally exerted on a battery will affect the performance of the battery and vice versa. Although all types of batteries are subject to mechanical stresses throughout their lifetime from fabrication processes, chemical reactions, and thermal expansions, the detrimental stress effects in this type of battery may be more significant than those in conventional batteries due to the load-bearing role of the structural battery. It is known with conventional batteries that the mechanical stresses may cause material

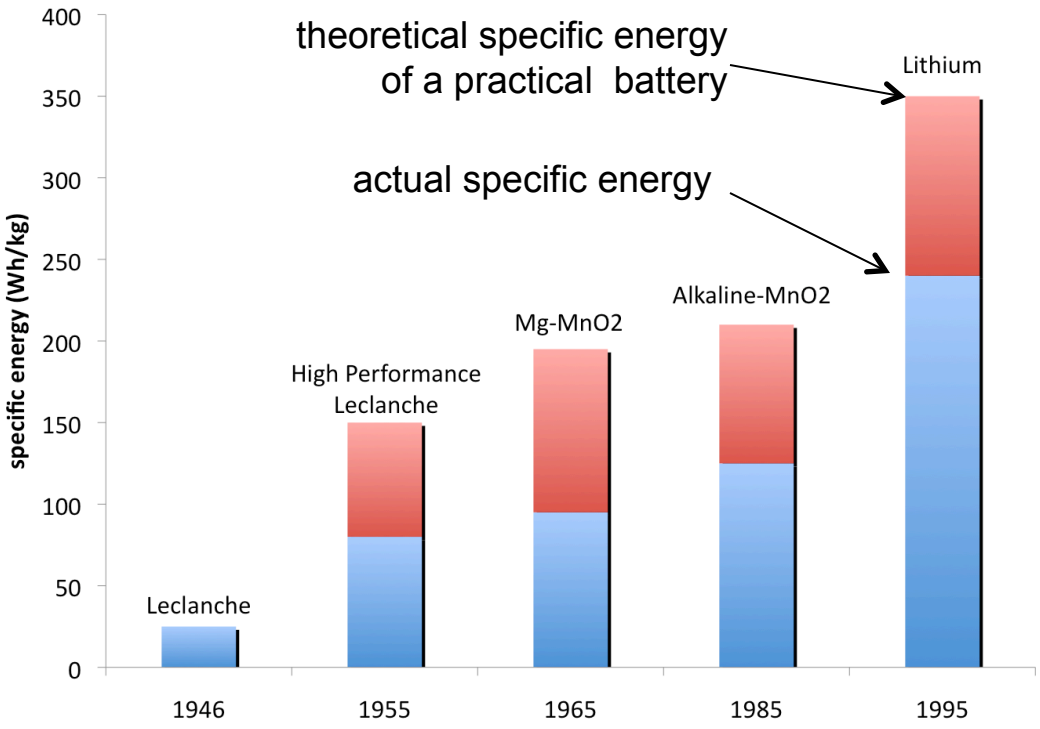

Figure 1.1: Advances in primary battery specific energy, adapted and modified from the reference [1]

failures, consequently shortening battery lifetime and also affect the performance while batteries are in use [2-4]. Since most previous works on the correlation between mechanical stresses and electrochemistry have used porous electrode materials, common in conventional batteries, they have observed the effects of particle packing during fabrication [2-4] or the stress generation due to charge-carrying ion transport [5-7], but certainly not the effects of externally applied stresses on a electrode material during operation as in a structural battery. Thus, in this work, the correlation between battery functions and mechanical stresses was investigated in experimental and computational ways, and the technical details were introduced in the following chapters.

Firstly, various sources of mechanical stresses present in batteries were reviewed in Chapter II. Stresses induced by structural loadings and thermal expansions were evaluated using finite element analysis on selected applications from a purely structural point of view without considerations on electrochemistry. These stresses, were then compared with those generated during fabrication and chemical reactions. Computational methods to assess fabrication and intercalation induced stresses were also briefly introduced. Significance of each type of stress on battery function was discussed.

In Chapter III, experiments on structural batteries are presented. A novel design of a structural battery was made to simultaneously conduct mechanical and electrochemical tests. Diffusion coefficients of lithium ions in carbon fiber electrodes as a measure of a battery power performance were determined while various levels of strains were applied. Also, stresses exerted on the battery were observed while the battery was electrochemically charged and discharged. The correlation between mechanical stress and battery function was discussed.

Molecular dynamics simulation was conducted to investigate the underlying mechanisms in findings of Chapter III. As in the experiments, graphite was deformed by prescribed strains and the change in diffusion coefficients as well as the reaction forces were calculated. Details of simulation are presented in Chapter IV.

In Chapter V, the major findings in the current work were summarized and future directions were suggested.

BIBLIOGRAPHY

1. Linden, D., 2001, "Ch. 1: Basic Concepts," in Handbook of batteries 3rd ed., D. Linden and T.B. Reddy ed., p.1.17, The McGraw-Hill Companies, Inc., New York.

2. Striebel, K.A., Sierra, A., Shim, J., Wang, C.-W., and Sastry, A.M., 2004, "The effect of compression on natural graphite anode performance and matrix conductivity," Journal of Power Sources, v.134, pp.241-251.

3. Wang, C.-W., Yi, Y.-B., Sastry, A.M., Shim, J. and Striebel, K.A., 2004, "Particle Compression and Conductivity in Li-ion Anodes with Graphite Additives," Journal of the Electrochemical Society, v. 151 (9), pp. 1489-1498.

4. Yi, Y.-B., Wang, C.-W. and Sastry, A.M., 2006, "Compression of Packed Particulate Systems: Simulations and Experiments in Graphitic Li-ion Anodes," ASME Journal of Engineering Materials and Technology, v. 128(1), pp. 73-80.

5. Choi, Y.-M., and Pyun, S.-I., 1997, "Effects of intercalation-induced stress on lithium transport through porous $LiCoO_2$ electrod," Solid State Ionics, v.99, pp.173-183.

6. Christensen, J., and Newman, J., 2006, "A Mathematical Model of Stress Generation and Fracture in Lithium Manganese Oxide," Journal of the Electrochemical Society, v. 153 (6), pp. A1019-A1030.

7. Zhang, X.-C., Shyy, W., and Sastry, A.M., 2007, "Numerical Simulation of Intercalation-Induced Stress in Li-Ion Battery Electrode Particles," Journal of the Electrochemical Society, v. 154 (10), pp. A910-A916.

CHAPTER II

MULTIFUNCTIONAL COMPOSITE MATERIALS: CONSIDERATION OF LOADS IN EMBEDDED AND INTEGRATED LI BATTERIES[1]

INTRODUCTION

Realization of the most novel power sources must necessarily invoke modeling capability, especially if these materials are expected to perform multiple roles, i.e. power generation and mechanical support. While the most promising electrochemical power supplies have only been realized with the ability to reproducibly fabricate high-surface area electrodes, which are necessarily composites, a structural battery can dramatically improve gravimetric/volumetric properties by removing parasitic masses that were unavoidable in conventional devices. Applications include satellites, unmanned aero-vehicles, and other military equipment where gravimetric properties are critical. Examples of pioneer work are WASP and PowerFiber where lithium ion batteries were integrated to wings and fabric, respectively [1]. Table 2.1 shows several types of battery-powered unmanned aero-vehicles in operation or under development along with their power requirement, mass distribution, and their missions. One can notice that battery/total mass ratio was significantly improved by utilizing battery as structural members in WASP.

[1] Material in this chapter is an unpublished paper in progress: H. C. Kim and A. M. Sastry, Multifunctional Composite Materials: Consideration of Loads in Embedded and Integrated Li Batteries, *Journal of Composite Materials* (2009).

project	type	mass (g)			mass ratio		required power (W)	battery		endurance	multi-functionality
		total	structure	battery	battery /total	battery /structure		electro-chemistry	capacity (mAh)		
Microbat [2]	ornithoper	12.5	2.6	3.0	0.24	1.15	0.27	Ni-Cd	50	42 sec	no
Mesicopter [3]	rotary wing	61.19	3.35	26.18	0.42	7.81	3.6	Ni-Cd	50	5 mins	no
Dragon Eye [4]	fixed wing	2040	363	635	0.31	1.75	120	Li-ion	6350	30-60 mins	no
WASP I [5]	fixed wing	82	9	41	0.5	4.56	11	LiSOCl2	1000	60 mins	yes

Table 2.1: Battery powered unmanned aero vehicle: component mass and power requirement.

Exploitation of structural batteries requires advanced analysis and simulation of mechanics and electrochemistry due to their interdisciplinary nature. For example, when structural batteries are in operations, they may be subject to various external loadings, which may affect electrochemical functions of batteries depending on applications. Here, we focus on evaluating various types of mechanical stress sources that may exist in batteries since mechanical failures of active materials in Li batteries are blamed for their lifetime limitation. Four different sources of mechanical stresses exerted on a battery were examined in this study: structural, thermal, fabrication and kinetics (Figure 2.1). Manufacturing loads are applied while battery electrodes are compressed to achieve desired volume fraction to improve their volumetric properties as well as conductivities. Heat generated by exothermic reactions and electrical resistance in batteries produces repetitive thermal expansion and contraction of the materials. Kinetic loads are due to chemical reactions in the battery. Lithium ion insertion into and extractions out of lattices of the active materials during charging or discharging causes the lattices to experience repetitive volume changes.

There have been theoretical and experimental efforts to identify failure mechanisms due to these mechanical loadings in battery active materials. A series of studies showed that compression of carbonaceous electrode materials during manufacturing not only improves their performances, but also can damage the materials, resulting conductivity decrease [6-8]. Mathematical models suggested that stresses induced during lithium ion insertion and extraction can be larger than the strength of the active materials [9, 10]. A numerical study revealed how particle size and aspect ratio affect stresses induced by intercalation in a $LiMn_2O_4$ particle [11]. Strains in battery

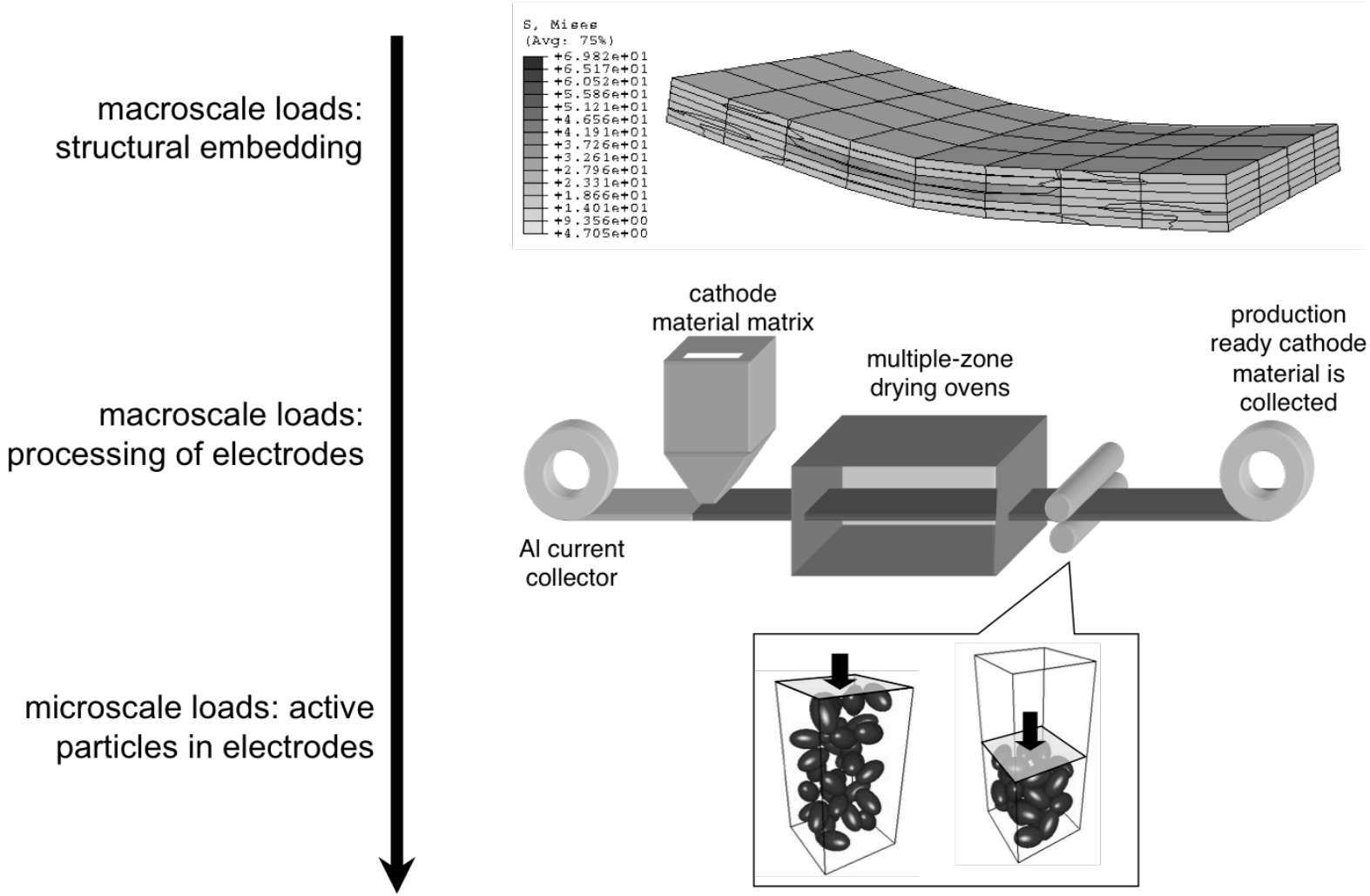

Figure 2.1: Structures and loads: Mechanical stresses in real world come from various sources including structural embedment, fabrication, and electrochemical reaction.

electrodes at macro-scale [12] and micro-fractures in active material particles have been empirically found [13-15].

Despite the numerous efforts to understand the mechanical stresses in batteries, there has been little attention paid to various sources of loadings applied to batteries, other than intercalation-induced stresses. This is probably because batteries in conventional applications are not intended to bear any structural load and assumed to be kept in a stress free environment. However, even batteries in conventional applications are subject to compressive loadings during fabrication. Evaluating possible sources of loads and designing batteries is thus important.

Our overarching objectives are to determine how materials architecture, electrochemistry, and charge/discharge processes influence load transfer within and outside the cell. In this study, as a preliminary step, we first aimed to systematically identify mechanical loads applied to batteries from various sources at different scales and quantify their relative contributions without considering the coupling effects of electrochemistry. The loadings at device scale were studied with selected structural battery applications, and the induced stresses at microscale were computed with particle models using finite element analysis.

METHODS

STRUCTURAL SIMULATIONS

Application scale finite element analysis was conducted to quantify loadings from structural and thermal sources. For a practical purpose, a micro air vehicle WASP and PowerFiber were chosen as examples to assess the level of external loadings in realistic

situations where structural batteries are employed. Loading and boundary conditions deduced from the examples were applied to simplified structure assuming the worst-case scenario.

Lifts on airfoil of WASP were obtained using two-dimensional CFD simulation using COMSOL multiphysics. The turbulent flow was modeled by the Reynolds-averaged Navier-Stokes equation as

$$\rho\frac{\partial \mathbf{U}}{\partial t} + \rho\mathbf{U}\cdot\nabla\mathbf{U} + \nabla\cdot(\rho\mathbf{u}\otimes\mathbf{u}) = -\nabla p + \nabla\cdot\eta\left(\nabla\mathbf{U} + (\nabla\mathbf{U})^T\right) + \mathbf{F}, \quad (1)$$

where ρ is the density, $\mathbf{U}$ is the averaged velocity field, $\mathbf{u}$ is the fluctuating part, and p and $\mathbf{F}$ are pressure and body force, respectively. Two additional closure relations relating the turbulence kinetic energy, k, and the dissipation rate of turbulence energy, ε, are

$$\boxed{\rho\frac{\partial k}{\partial t} - \nabla\cdot\left[\left(\eta + \frac{\eta_T}{\lambda_k}\right)\nabla k\right] + \rho\mathbf{U}\cdot\nabla k = \frac{1}{2}\eta_T\left(\nabla\mathbf{U} + (\nabla\mathbf{U})^T\right)^2 - \rho\varepsilon,} \text{ and} \quad (2)$$

$$\rho\frac{\partial \varepsilon}{\partial t} - \nabla\cdot\left[\left(\eta + \frac{\eta_T}{\lambda_\varepsilon}\right)\nabla\varepsilon\right] + \rho\mathbf{U}\cdot\nabla\varepsilon = \frac{1}{2}C_{\varepsilon 1}\frac{\varepsilon}{k}\eta_T\left(\nabla\mathbf{U} + (\nabla\mathbf{U})^T\right)^2 - \rho C_{\varepsilon 2}\frac{\varepsilon^2}{k}, \quad (3)$$

where η and η_T are respectively dynamic and turbulent viscosity, and C and λ are model constants determined experimentally. For this analysis, the general purpose Clark Y type airfoil was used with the chord length 15 cm and the angle-of-attack 10 degree. The size of the simulation domain was 1 m x 1 m. The velocity of the inlet airflow was 14 m/s, the outlet pressure was set to zero, and all the rest boundaries had no-slip conditions. The pressure obtained in the CFD analysis was then introduced to the structure analysis as loading conditions.

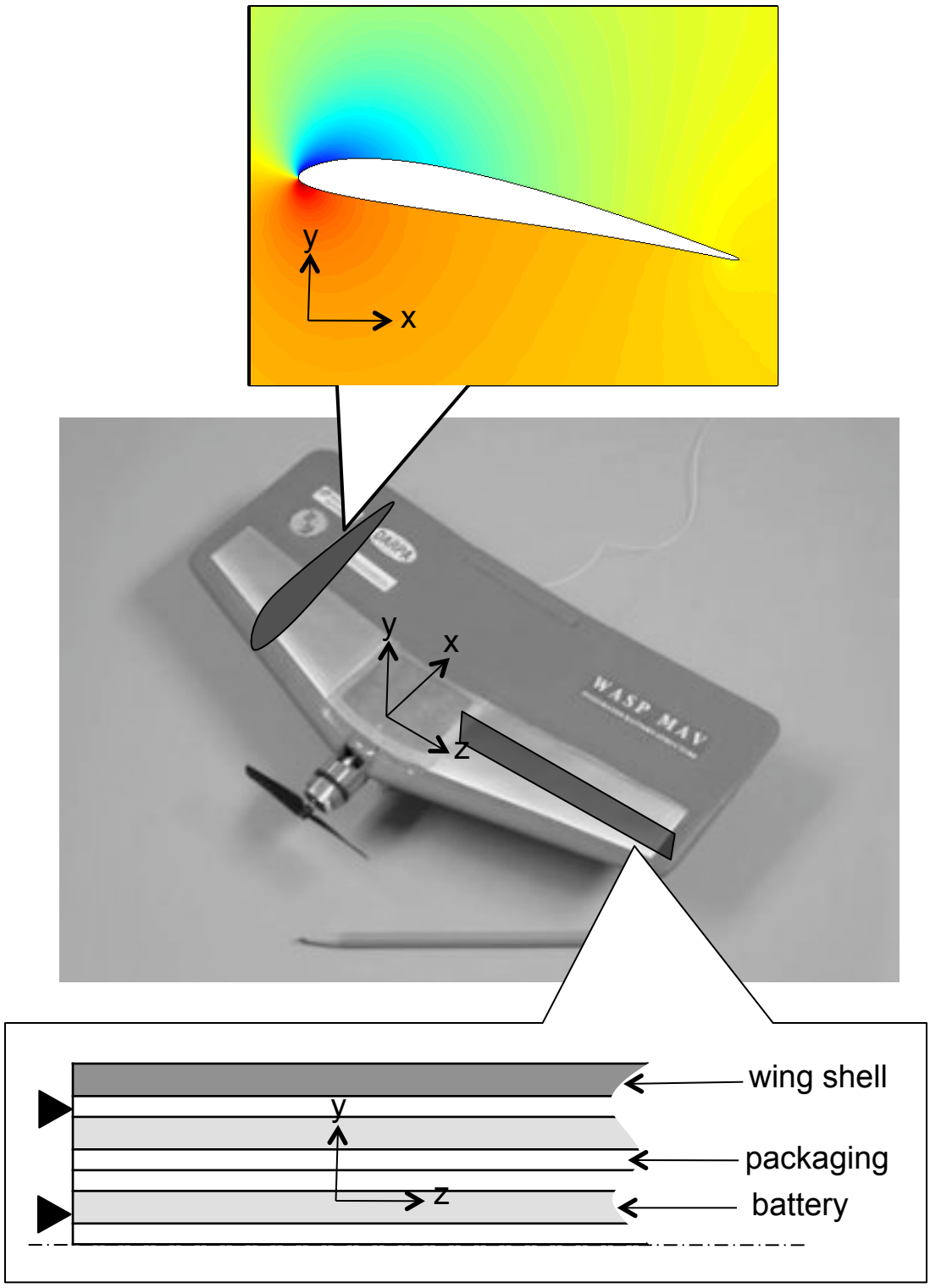

Figure 2.2: WASP (callout) plane strain beam model showing layered structure.

In the structural analysis, two-dimensional plane strain beam was constructed. The cross section of the beam in Figure 2.2 shows layers of materials in the wingspan direction. The cells enclosed in polymer packaging were placed between two Styrofoam shells. Mechanical and thermal material properties used in this model are listed in Table 2.2. Mechanical loading and thermal loading were exclusively applied. When structural loading was considered, one end of the beam close to the fuselage was structurally fixed and the maximum pressures obtained from CFD analysis were applied to the top and the bottom surface of the beam. When the thermal loading was in consideration, constant temperature, 300K was prescribed at the fuselage side end, and convective heat transfer to flowing air was prescribed with coefficient h = 20 W/m^2K at all the rest boundaries. Constant heat sources, $1000W/m^3$ were designated to the battery layers. The steady state heat transfer problem was fist solved and the resulting temperature field was used for further thermal-structure analysis as shown in the following equations.

$$\mathbf{e}_{thermal} = \mathbf{a}\left(T - T_{ref}\right), \text{ and} \tag{4}$$

$$\mathbf{s}_{thermal} = \mathbf{E}\left(-\mathbf{e}_{thermal}\right), \tag{5}$$

where $\mathbf{s}$ and $\mathbf{e}$ are stress and strain tensor, and $\mathbf{a}$, T, $\mathbf{E}$ are thermal expansion coefficients tensor, temperature, and stiffness tensor, respectively.

Similarly, an FEM model of PowerFiber was constructed using COMSOL. As shown in the reference [16], the PowerFiber can be embedded in polymer resin to be used as PowerComposite. In this configuration, the fibers may experience bending and torsion as a flat PowerComposite ribbon is twisted. To simulate this condition, a 100 μm long fiber was subject to prescribed boundary conditions mimicking the ribbon under torsion

layer	material	thickness (mm)	elastic modulus (MPa)	thermal conductivity (W/m•K)*	thermal expansion coefficient (1/K)*	heat capacity (J/kg K)*
wing shell	polystyrene	0.92	127	0.1	$8x10^{-5}$	1300
battery packaging	Dai-Nippon EL-40	0.11	4604	0.12	$3.2x10^{-5}$	2000
battery	Telcordia PLI	0.54	1020	4[Takahata]	$1.0x10^{-6}$	800

Table 2.2: Thickness and material properties of layers in WASP wing.

and bending by 90 degrees from its reference state. For thermal loading simulation, the active materials in the fiber were designated as heat source, and the outer surface was exposed to free convection of air with h = 10 W/m^2K. The detailed composition of materials and their properties are described in Figure 2.3 and Table 2.3, respectively.

MICRO-STRUCTURAL SIMULATIONS

Loads on particles in electrodes due to rolling process during fabrication can be determined with compression simulation. For this simulation, 1000 spherical particles were randomly distributed in a box with rigid walls as seen in Figure 2.4. Then the particles were compressed to achieve a certain volume fraction, typically 60% in commercial batteries (Figure 2.1 bottom). $LiMn_2O_4$ was used as a cathode material in this study, the mean diameter was 8.96 μm, the elastic modulus was 10 GPa and the simulation domain size was 224 μm x 224 μm x 672 μm (Table 2.4). Friction coefficient between particles and between particles and walls were set to zero. More detailed descriptions on computation can also be found in the reference [8].

Stresses due to kinetics of chemical reactions in batteries were determined using a single particle simulation. Intercalation-induced stresses were formulated as an analogy to thermal stresses in the elasticity as shown by

$$\mathbf{e} = \mathbf{E}^{-1}\left[(1+\nu)\mathbf{s} - \nu\,\mathrm{trace}(\mathbf{s})\mathbf{I}\right] + \frac{\Delta c \Omega}{3}\mathbf{I}, \tag{6}$$

where ν is the Poisson's ratio, c is the concentration of the diffusion species, and Ω is the partial molar volume of the species. Then the generalized diffusion equation was coupled to incorporate electrochemical processes as

$$\frac{\partial c}{\partial t} = -D\left(\nabla c - \frac{c\Omega}{RT}\nabla\sigma_h\right), \tag{7}$$

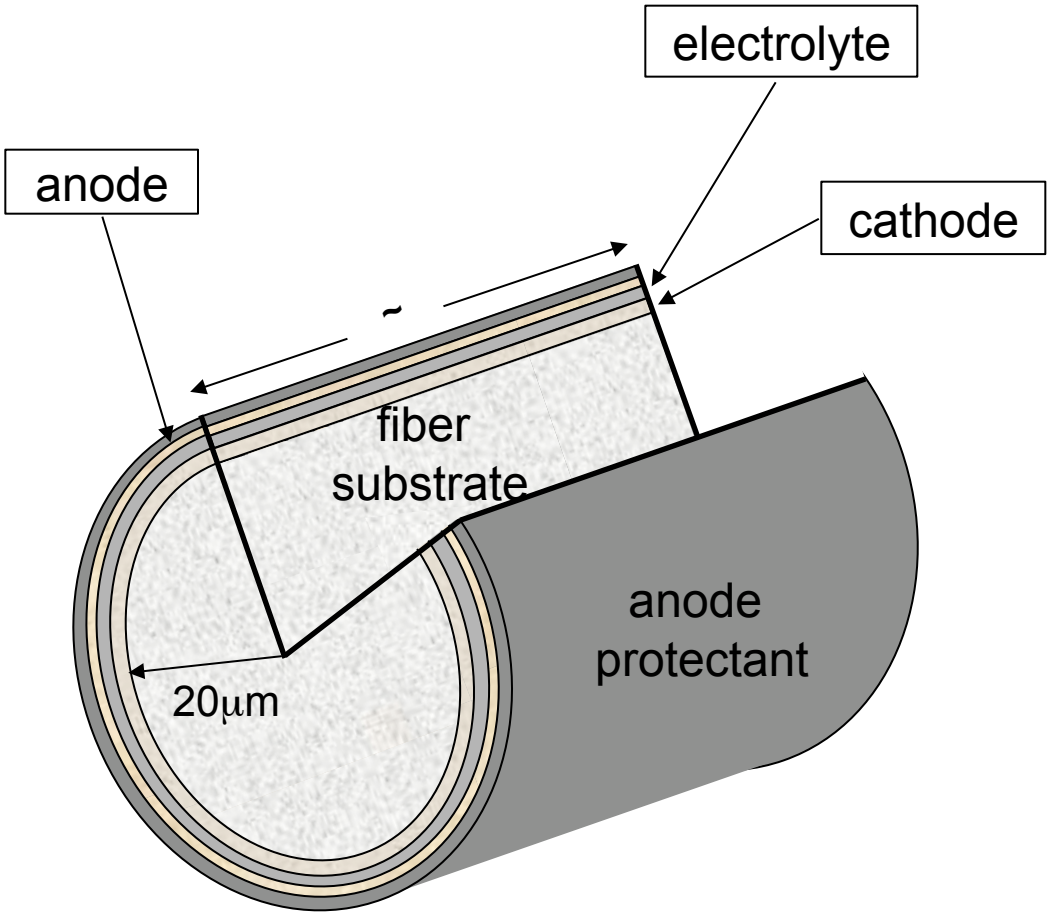

Figure 2.3: Layered structure of PowerFiber.

layer	material	thickness (μm)	modulus (GPa)	thermal conductivity (W/m K)	thermal expansion coefficient (1/K)	heat capacity (J/kg K)
fiber substrate	stainless steel	40	200	20	17.3×10^{-6}	500
cathode	$Li_{1.6}Mn_{1.8}O_4$	1	10	10*	10×10^{-6}*	800*
electrolyte	$Li_{3.1}PO_{3.3}N_{0.5}$	2	10*	10*	10×10^{-6}*	800*
anode	Sn_3N_4	1	30	10*	10×10^{-6}*	800*
anode protectant	Cu	1	120	400	16.5×10^{-6}	385

Table 2.3: Thickness and material properties of layers in PowerFiber.

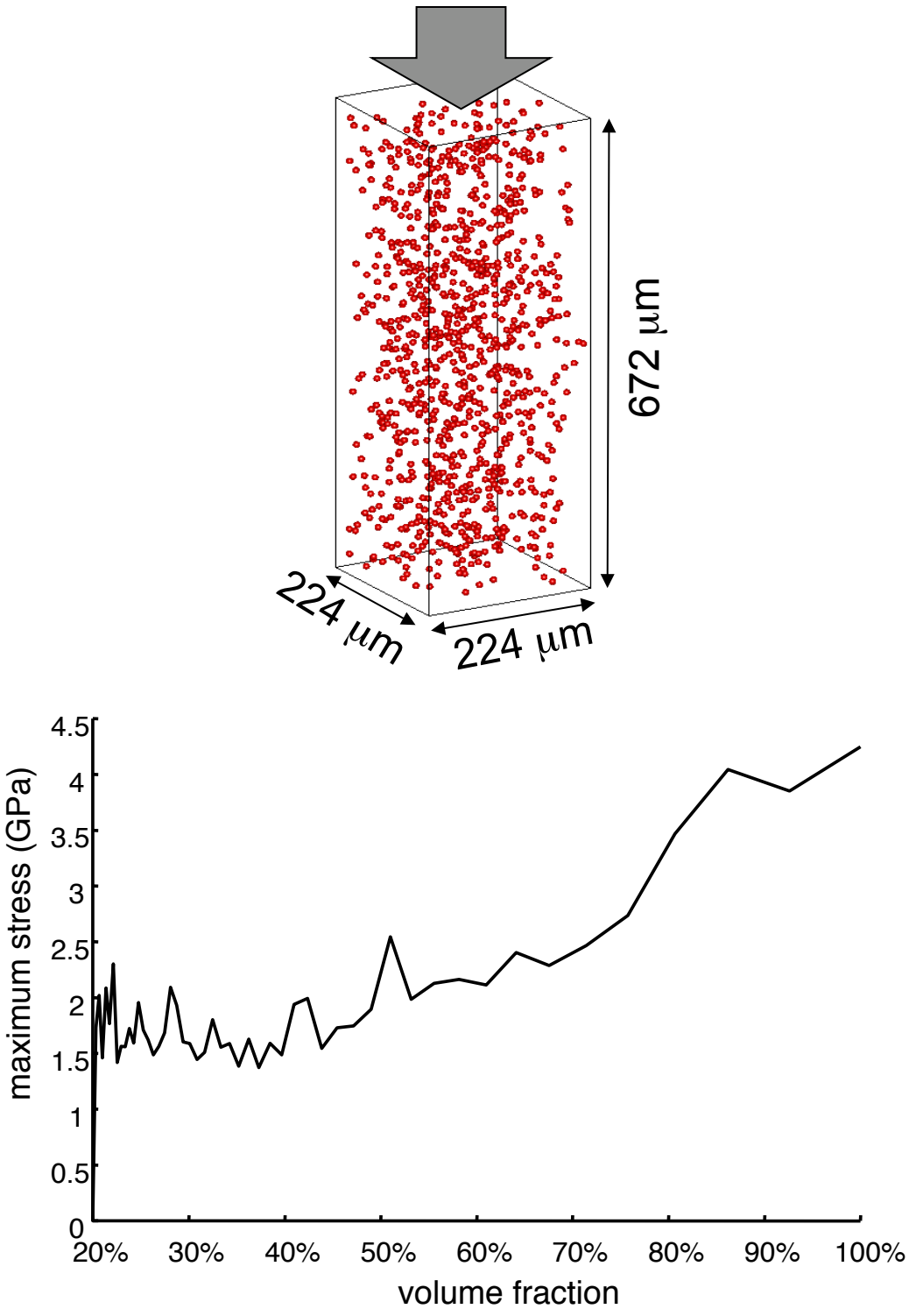

Figure 2.4: (top) Compression model of particulate electrode
(bottom) maximum von Mises stress vs. volume fraction of active material.

material	$LiMn_2O_4$
particle size (μm)	8.96
modulus (GPa)	10
cell size (μm^3)	224×224×672
diffusion coefficient (m^2/s)	7.08×10^{-15}
stoichiometric maximum concentration (mol/m^3)	2.29×10^{4}
partial molar volume (m^3/mol)	3.497×10^{-6}

Table 2.4: Material properties and simulation configurations used for micro-scale simulation.

where t is time, D is the diffusion coefficient, R is the universal gas constant, and σ_h is the hydrostatic stress. A $LiMn_2O_4$ particle was studied with respect to various discharge current densities, particle sizes, and aspect ratios. The computation was done with COMSOL Mutiphysics. Material properties used in this model are listed in Table 2.4. More detailed descriptions can be found in the reference [11].

RESULTS

Finite element analysis simulations showed that structural battery applications including WASP and PowerFiber exhibited maximum von Mises stresses in the range of 0.2 ~ 0.5 MPa in their battery portions while conducting their typical missions (Table 2.5). Though there were larger stress values in the structures than these values, stresses in the battery portion were considered here since battery material was our prior concern. Stresses induced by specific type of structural loadings are shown in Figure 2.5, 2.6 and 2.7 and the maximum stress values were in the same order among different cases.

Thermal stresses in the applications, on the other hand, were not only one or two orders of magnitude larger than those by structural loadings, but also were different from WASP to PowerFiber. WASP had about 9 MPa of maximum von Mises stresses induced by thermal expansion throughout batteries imbedded in the layered wing structure and PowerFiber had 100 MPa of maximum von Mises stress in the anode portion (Table 2.5, Figure 2.8 and 2.9).

In microscopic simulations, single $LiMn_2O_4$ particle had von Mises stress as large as 2000 MPa due to compression (Table 2.5, Figure 2.4). This value is several orders larger than those from structural loading case. Lithium intercalation into the cathode

sources		maximum von Mises stress (MPa)
external / structural	WASP	0.2
	PowerFiber (bending / torsion)	0.5 / 0.4
thermal	WASP	9
	PowerFiber	100
manufacturing		2000
intercalation		45

Table 2.5: Maximum von Mises stresses from various sources.

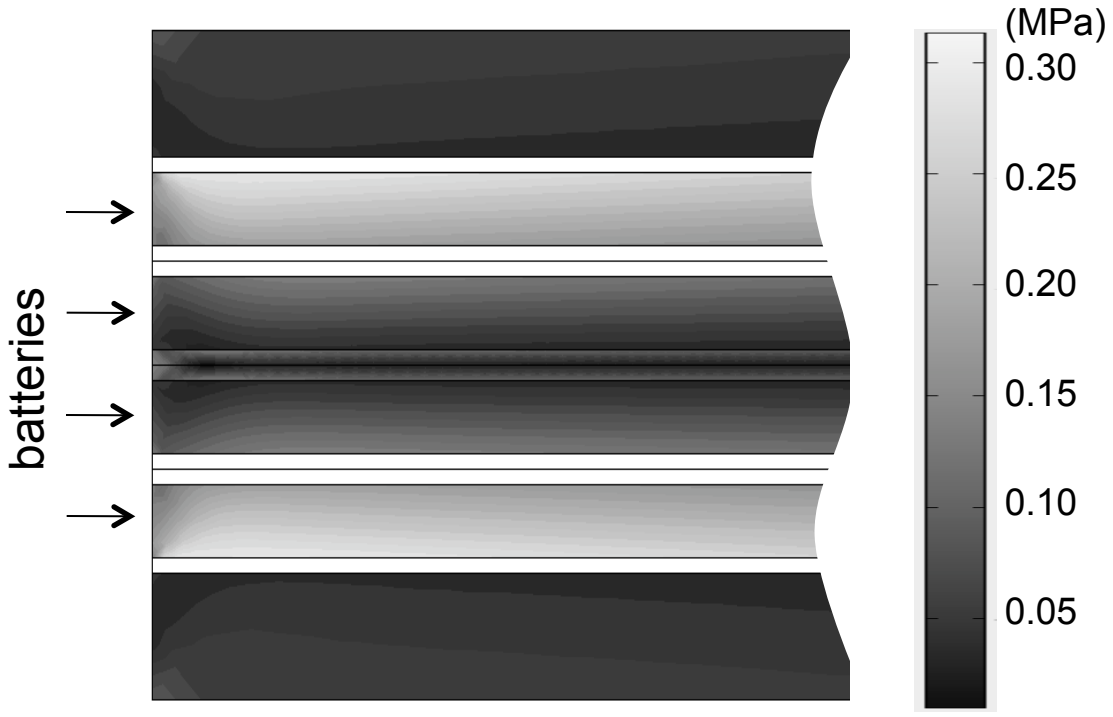

Figure 2.5: Maximum von Mises stress distribution due to structural loadings in WASP wing section.

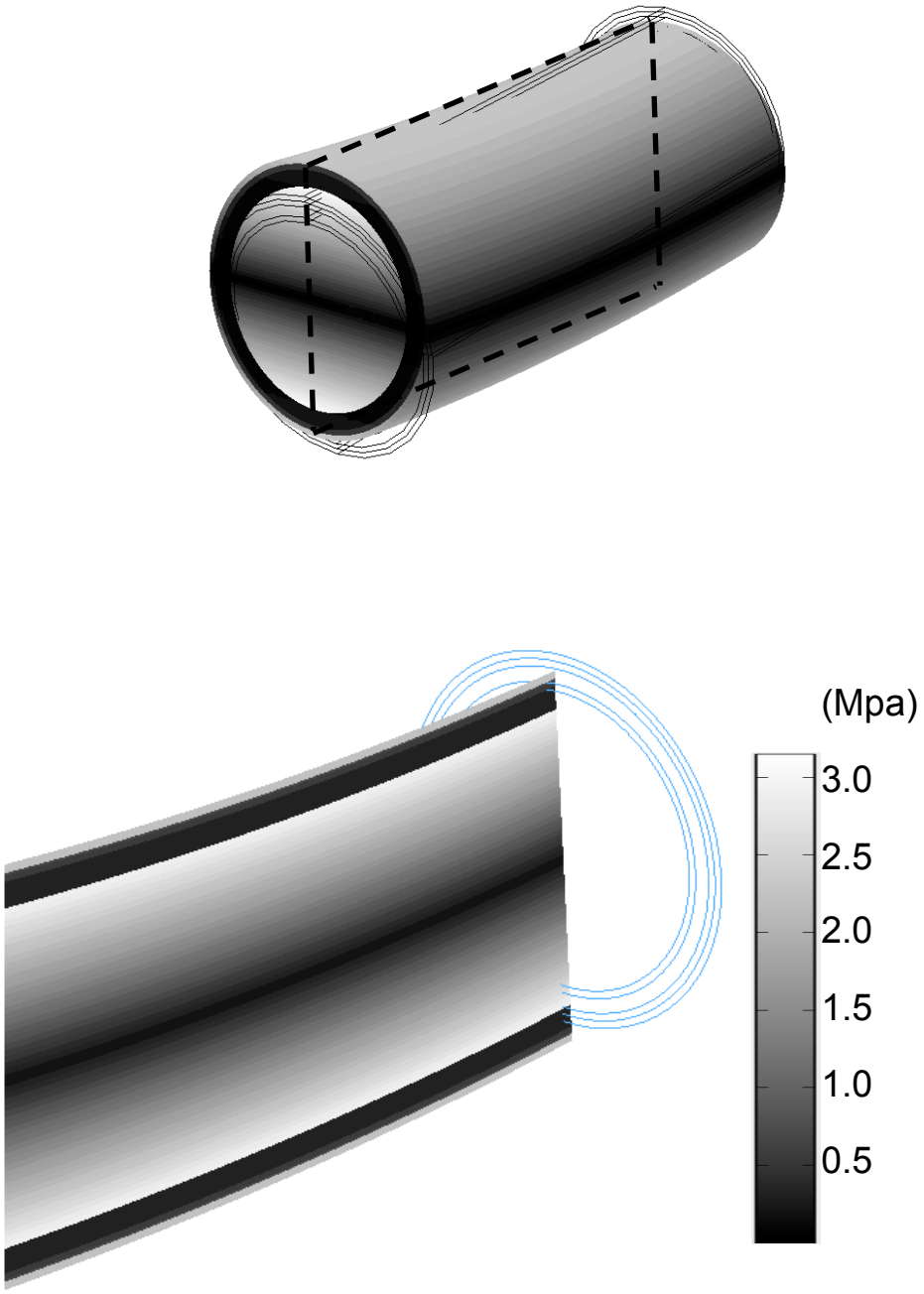

Figure 2.6: Maximum von Mises stress distribution due to structural loadings in PowerFiber under bending.

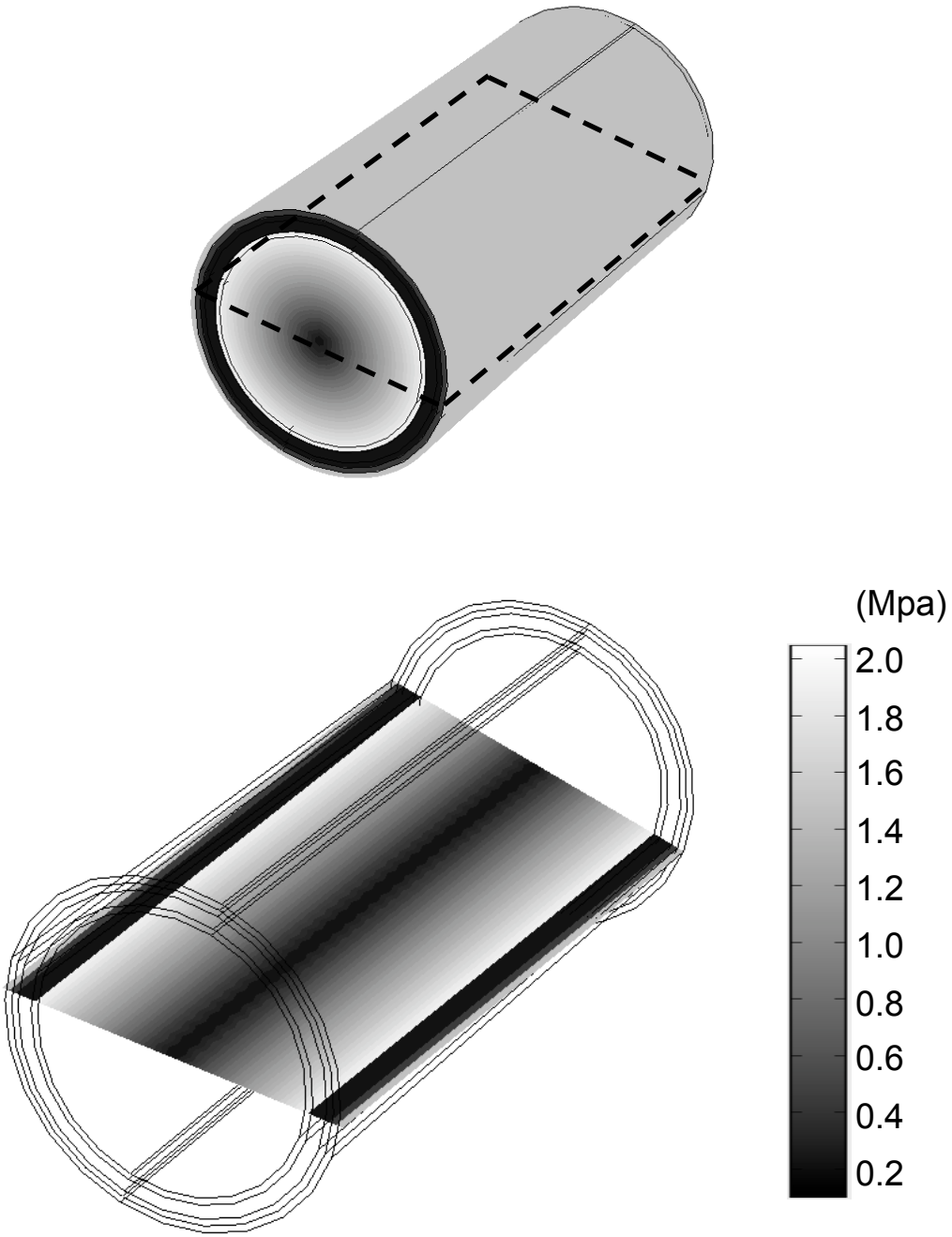

Figure 2.7: Maximum von Mises stress distribution due to structural loadings in PowerFiber under torsion.

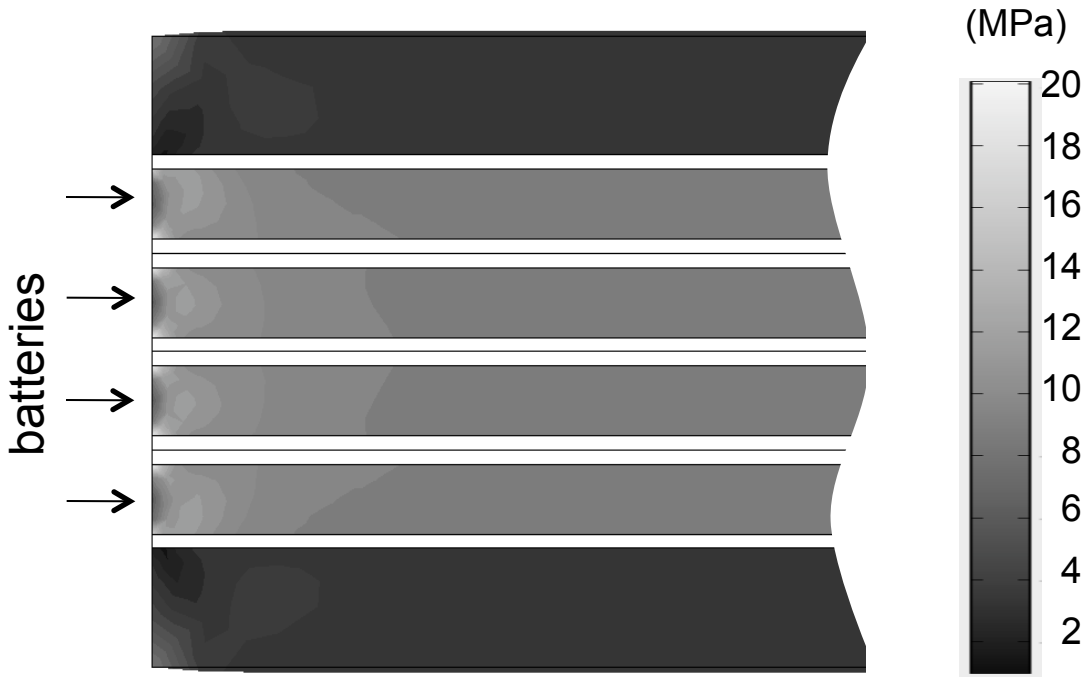

Figure 2.8: Maximum von Mises stress distribution due to thermal expansion in WASP.

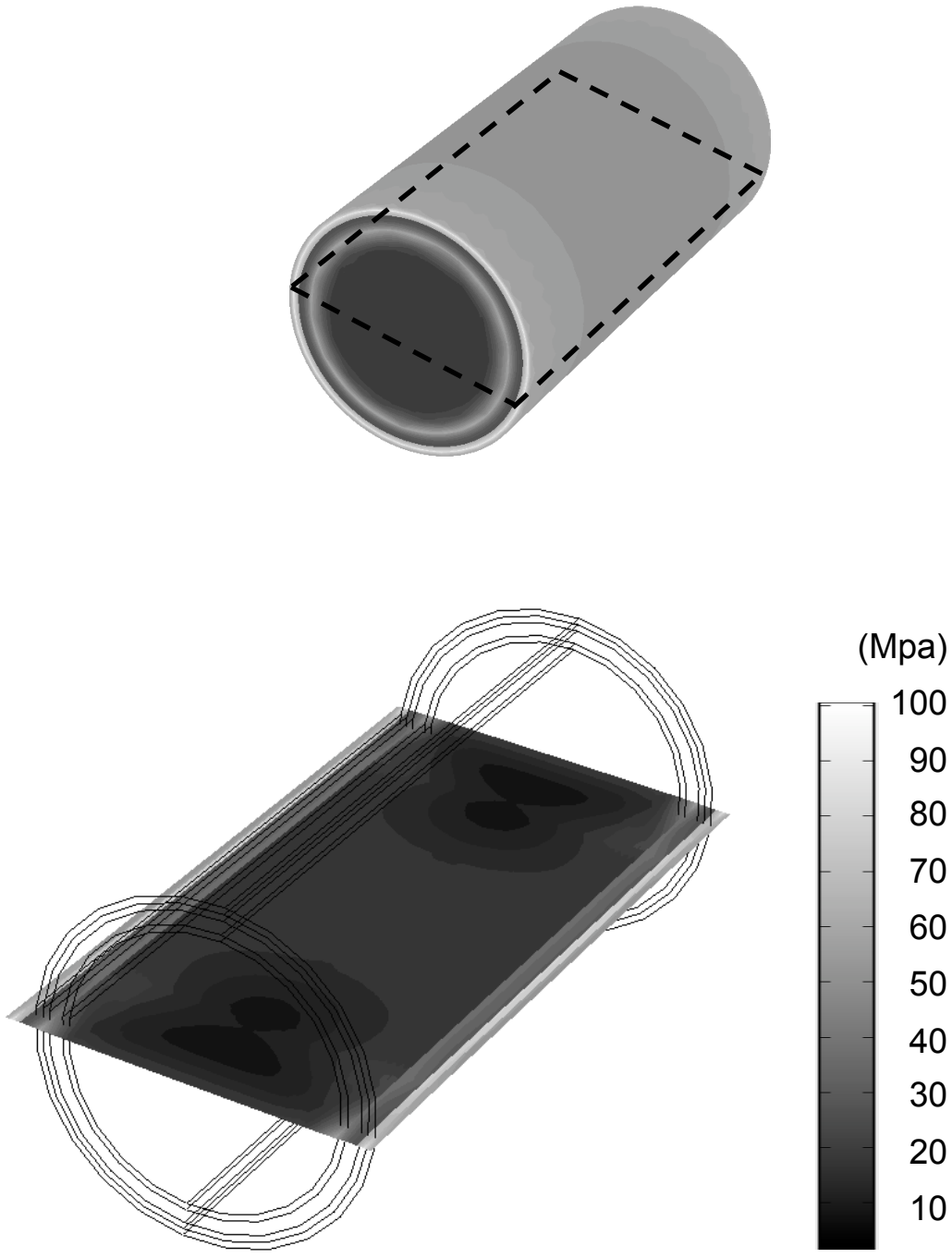

Figure 2.9: Maximum von Mises stress distribution due to thermal expansion in PowerFiber.

particle induced about 45 MPa of von Mises stresses when the aspect ratio of the particles remained between 1 and 2 (Table 2.5).

DISCUSSION

Stresses induced by structural loadings were relatively low compared to other sources of stresses. This is likely because structural batteries are mostly light duty applications and they adopt composite structures. For an example, pressures exerted on WASP wings are naturally low (O(100Pa)) due to lightweight of the vehicle and low speed (<15m/s) during mission. Also, layered composite structure helps batteries avoid large stresses by diverting those to reinforcement.

However, thermal expansion in PowerFiber produced significant stresses. Since ultimate strength in most oxide materials is about 100 MPa [10], the thermal stresses in this case may cause material failure, resulting in failure as power storage. This relatively high stress was also caused by layered structure. Differently from the structural loading case, reinforcement materials with higher elastic modulus functioned as rigid confinement. Thus, when designing structural batteries, not only beneficial features of composites such as lightweight and high strength, but also their adverse effects as stress sources when combined with thermal expansion should be carefully considered.

Micro-scale simulation showed that the maximum stresses during particle compression up to volume fraction 60% reached 2 GPa, much higher than the material strength. Since the simulation assumed that particles are perfectly sphere and all in the same size, the actual electrode particles with various sizes and aspect ratios would have lower stress than predicted. Nonetheless, the stresses during fabrication are considered as

a critical source which causes mechanical failure of particles [8]. However, compression process during fabrication can be avoided if electrodes are made as thin films as in PowerFiber using various deposition techniques.

CONCLUSIONS AND FUTURE WORK

Four different sources of mechanical stresses exerted on a battery implemented in a structure were examined in this study: structural, thermal, fabrication and kinetics. Finite element analysis showed that compression of conventional particulate electrode material would produce stresses as high as 2 GPa and thermal expansion of batteries embedded in a structure had stress of 100 MPa. Considering strength of typical oxide materials, these values may cause mechanical failure in electrode particles. On the other hand, stresses due to structural loadings and intercalation kinetics were relatively low, ranging from 0.2 to 45 MPa. Reinforcement materials in composite structures function as load bearing component when structural loading was applied, but as rigid constraint, leading to critical stresses when thermal loading was considered. Also, in a structural battery, the stresses exerted to the structure can be altered as large as 20 % of the initially applied value during charge/discharge cycles of the battery. Thus, when designing structural battery applications, one needs to consider the trade-offs in functions of reinforcement in composites as well as the influence of electrochemistry to the structural stability.

BIBLIOGRAPHY

8. Christodoulou, L. and Venables, J.D. (2003). Multifunctional Material Systems: The First Generation, JOM, 55: 39-45.

9. Pornsin-Sirirak, T.N., Tai, Y.C., Ho, C.H. and Keenon, M. (2001). Microbat-A Palm-Sized Electrically Powered Ornithopter, NASA/JPL Workshop on Biomorphic Robotics, Pasadena, CA.

10. Kroo, I., Shantz, M., Kunz, P., Fay, G., Cheng, S., Fabian, T., and Partridge, C. (2000). The Mesicopter: A Miniature Rotorcraft Concept, Phase II Interim Report, http://adg.stanford.edu/mesicopter.

11. Foch, R.J. (2001), Dragon Eye, Airborne Sensor System for Small Units, Solicitation No. N00173-01-R-MS01, Attachment 6, NRL Code 5712, http://heron.nrl.navy.mil/contracts/closed/01ms01/presentation.pps.

12. Thomas, J.P., Qidwai, M.A., Matic, P., Everett, R.K., Gozdz, A.S., Keennon, M.T., and Grasmeyer, J.M. (2002). Multifunctional Structure-Plus-Power Concepts, 43rd AIAA/ASME/ASCE/AHS/ASC Structures, Structural Dynamics, and Materials Con., Denver, Colorado, AIAA 2002-1239.

13. Striebel, K.A., Sierra, A., Shim, J., Wang, C.-W. and Sastry, A.M. (2004). The Effect of Compression on Natural Graphite Anode Performance and Matrix Conductivity, Journal of Power Sources, 134(2): 241-251.

14. Wang, C.-W., Yi, Y.-B., Sastry, A.M., Shim, J. and Striebel, K.A. (2004). Particle Compression and Conductivity in Li-ion Anodes with Graphite Additives, Journal of the Electrochemical Society, 151(9): 1489-1498.

15. Yi, Y.-B., Wang, C.-W. and Sastry, A.M. (2006). Compression of Packed Particulate Systems: Simulations and Experiments in Graphitic Li-ion Anodes, ASME Journal of Engineering Materials and Technology, 128(1): 73-80.

16. Christensen, J. and Newman, J. (2006). Stress generation and fracture in lithium insertion materials, Journal of Solid State Electrochemistry, 10(5): 293-319.

17. Christensen, J. and Newman, J. (2006). A mathematical model of stress generation and fracture in lithium manganese oxide, Journal of Electrochemical Society, 153(6): A1019-A1030.

18. Zhang, X., Shyy, W., and Sastry, A.M. (2007). Numerical Simulation of Intercalation-Induced Stress in Li-Ion Battery Electrode Particles, Journal of The Electrochemical Society, 154(10): A910-A916.

19. Hahn, M., Buqa, H., Ruch, P.W., Goers, D., Spahr, M.E., Ufheil, J., Novak, P., and Kotz, R. (2008). A Dilatometric Study of Lithium Intercalation into Powder-

Type Graphite Electrodes, Electrochemical and Solid-State Letters, 11(9): A151-A154.

20. Wang, H., Jang, Y.-I, Huang, B., Sadoway, D.R., and Chiang, Y.-M. (1999). TEM Study of Electrochemical Cycling-Induced Damage and Disorder in LiCoO2 Cathodes for Rechargeable Lithium Batteries, Journal of The Electrochemical Society, 146(2): 473-480.

21. Lim, M.-R., Cho, W.-I., Kim, K.-B. (2001). Preparation and characterization of gold-codeposited LiMn2O4 electrodes, Journal of Power Sources, 92:168-176.

22. Wang, D., Wu, X., Wang, Z., and Chen, L. (2005). Cracking causing cyclic instability of LiFePO4 cathode material, Journal of Power Sources, 140:125-128.

23. Neudecker, B.J., Benson, M.H., and Emerson, B.K. (2003). Powerfibers: thin-film batteries on fiber substrates, In: Proceedings of the 14th international conference on composite materials (ICCM 14), Society of Manufacturing Engineers, San Diego, CA.

CHAPTER III

COUPLING EFFECTS OF MECHANICAL STRESSES AND ELECTROCHEMICAL CYCLES IN A CARBON FIBER LITHIUM ION BATTERY: EXPERIMENTAL STUDY[2]

INTRODUCTION

Batteries are under various mechanical stresses during fabrication due to material preparations and assembly with compression processes and while performing their duties owing to chemical reactions, thermal expansions, and external loadings. These stresses not only cause failure of batteries, limiting their lifetime, but also possibly affect their performances even during their lifetime. Here, the performance can be described as energy and power density and both densities are the key parameters to be improved for applications requiring high energy and power such as electric vehicles. Thus, understanding how mechanical stresses affect battery performances may help us reduce factors detrimental to battery performance and further architect a material structure in a desired way.

Work on the effect of mechanical stresses on battery functions has been mostly done with graphite electrode under compressive loadings. Conductivity and formation cycle of compressed natural graphite were examined and it was found that cyclability tends to improve with compression mainly due to improvement of conductivity [1].

[2] Material in this chapter is an unpublished paper in progress: H. C. Kim and A. M. Sastry, Coupling Effects of Mechanical Stresses and electrochemical cycles in a Carbon Fiber Lithium Ion battery: Experimental Study, *Journal of the Electrochemical Society* (2009).

Experiments coupled with computer simulations also showed that the improvement of conductivity originated from the decreased contact resistance between active materials and the current collector, and excessive pressure caused particle breakages [2]. This work was extended to include friction, morphology, and deformability of particles, and estimated friction coefficient and pressure at failure in real system [3]. Choi and Pyun discussed contact resistance and lithium ion diffusivity in $LiCoO_2$ as a function of lithium intercalation induced stress and found that the ion diffusivity decreased as intercalation induced stress increased [4].

Despite there have been a series of studies on this topic, it has not been possible to identify the direct correlation between mechanical stresses and battery functions. This is probably because all the previous work dealt with porous materials. In porous materials, the applied stresses largely alternate the packing state of multi-particulate systems rather than the actual active materials.

Thus, our goal in this work was to examine the direct correlation between mechanical stresses and battery performances, especially as results of deformation of active materials, not porosities. For this study, we aimed to achieve the following specific objectives:

1. To devise and fabricate lithium batteries which enable us to directly apply mechanical stresses to the active materials in the system.

2. To conduct coupled mechanical and electrochemical experiments to investigate the relationship between mechanical stresses and battery performances.

3. To understand the underlying mechanisms in this correlation.

METHODS

A half-cell was constructed with carbon fibers as a working electrode and metal lithium as a counter and reference electrode. The battery was encased in a plastic tube with parts of carbon fiber exposed to the environment for mechanical testing while keeping the materials inside of the battery safe from the moisture and oxygen.

MATERIALS AND BATTERY CONFIGURATION

Pitch based carbon fiber DIALEAD®-K13D2U was received from Mitsubishi Chemical Inc. A tow of fiber consists of 2000 filaments of the diameter, 11 μm. The yield of a tow is 2702 m/kg and the ultimate elongation is 0.4 %. Tensile modulus and strength are 935 GPa and 3700 MPa, respectively and thermal conductivity is over 800 W/mK. The fibers were sized with epoxy resin by 2 % of the total mass, and then cut into 16 cm long piece. Then two 1 cm wide bands separated by 4 cm between them around the center of the tow were coated with polyethylene (PE) to prevent leaking of electrolyte due to capillary effect. The center 4 cm between the coated bands was carefully kept intact from PE to be used as active materials. The center part of the tow was wrapped with a separator, Celgard® 3401, a lithium foil (99.9%, 40 mm × 12 mm × 0.38 mm, Sigma-Aldrich®), and a copper wire as a current collector, sequentially. This assembly was placed in a PE tube of ¼ inch inner diameter and 6 cm length. Gaps between the tube and the carbon fiber at both ends were heat sealed with PE glue after introducing electrolyte, 1M $LiPF_6$ in Ethylene Carbonate (EC, 99%, anhydrous, Sigma-Aldrich®) + Diethyl Carbonate (DEC, +99%, anhydrous, Sigma-Aldrich®) (Figure 3.1). The entire

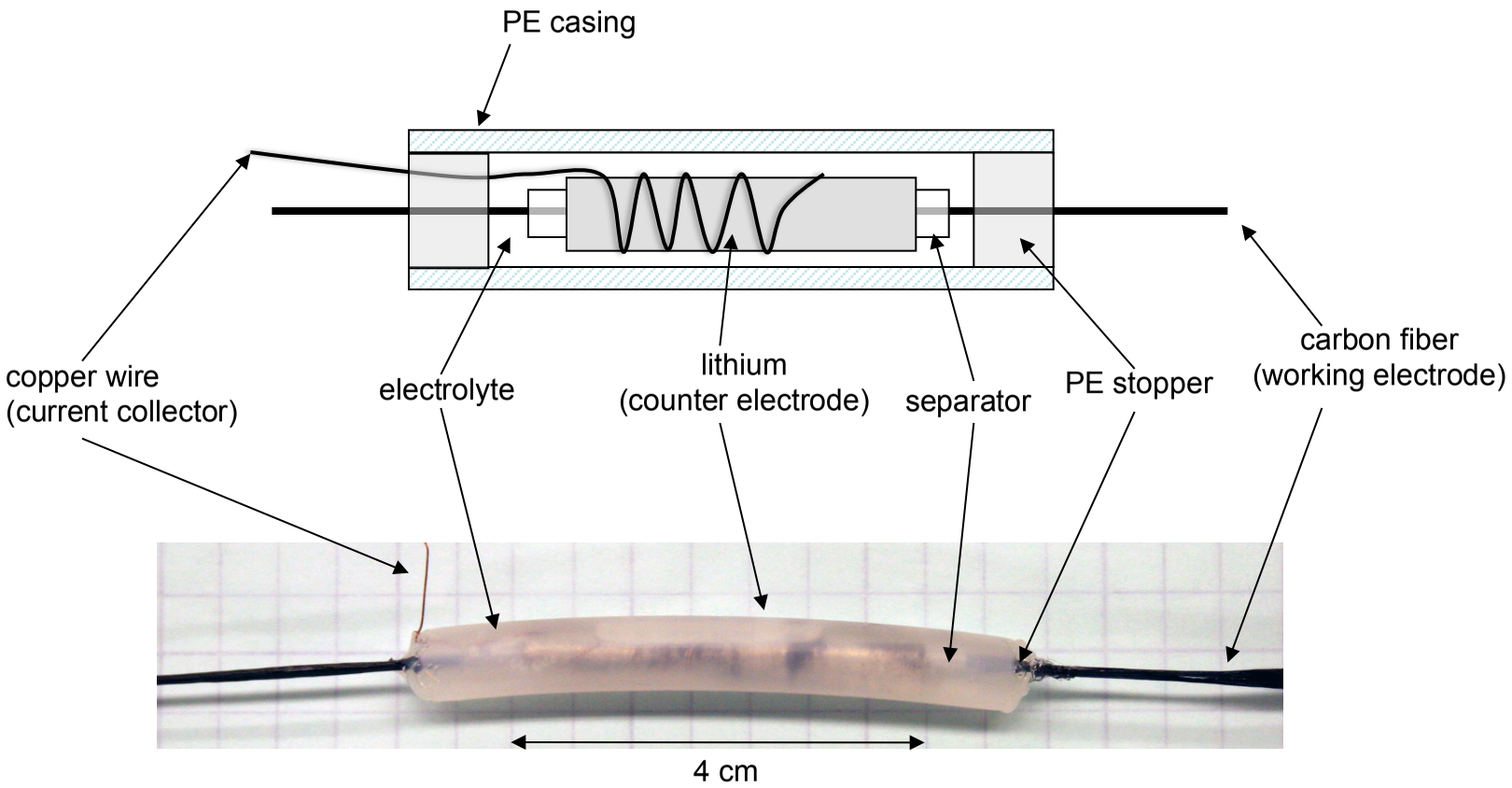

Figure 3.1:schematic of battery configuration and fabricated battery.

process was done in an argon-filled glove box. The moisture and oxygen level was maintained below 1 ppm.

EXPERIMENT SETUP AND MECHANICAL TESTS

Both carbon fiber ends extruding out of the battery were fixed in wooden blocks with epoxy for mechanical test grip (Figure 3.2). Then the battery was loaded in the universal material tester, Instron® 3366 and also connected to the potentiostat Biologic VMP®3. Since a carbon fiber tow contains 2000 filaments, all the filaments could not be aligned so that they can be evenly strained by the equal amount. Instead, the fibers were strained until the applied load reached a certain value, say 50 N, then the point where most fibers were engaged with the tension was found from the load-elongation curve (Figure 3.3). Then the engagement point was recorded, and the cross head of the material tester was returned to the starting point. When we applied different values of strains, this engagement point was used as a pre-strain so that the actual elongation was the sum of the pre-strain and the strain we set as an experiment level. Electrochemical tests were done while 0, 0.15, and 0.3 % of strain were applied to the battery.

ELECTROCHEMICAL TECHNIQUES

Two basic electrochemical techniques were used in this study: galvanostatic cycling (GC) and cyclic voltammetry (CV). In GC, changes in potential of a battery are measured while it is charged/discharged with a constantly imposed current (Figure 3.4). Using this technique, the actual capacity of a battery can be obtained by the product of the imposed current and the elapsed time. In CV, potential of a battery is controlled

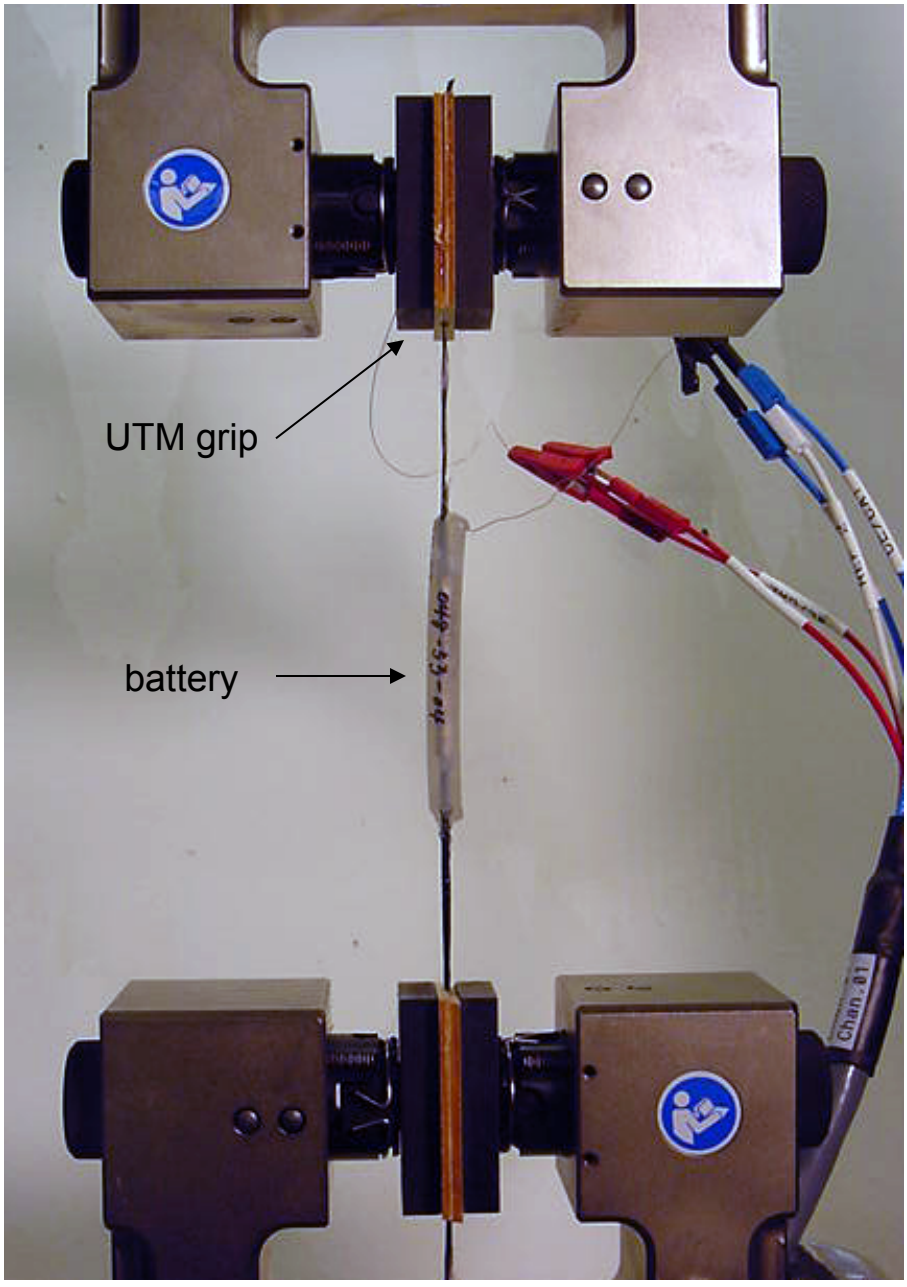

Figure 3.2: battery loaded in a material tester and connected to a potentiostat .

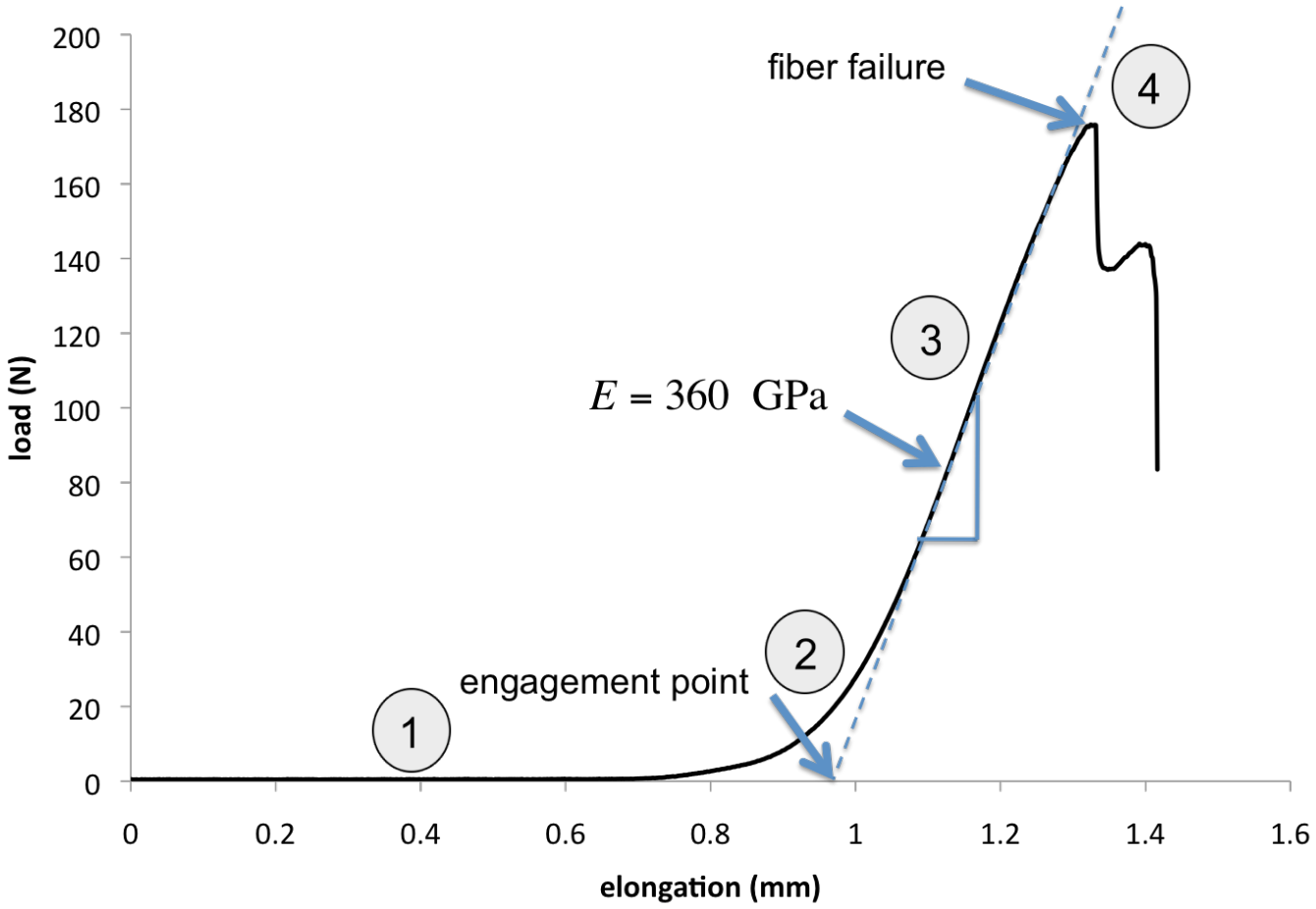

Figure 3.3 (a): load-elongation curve of battery under uni-axial tension.

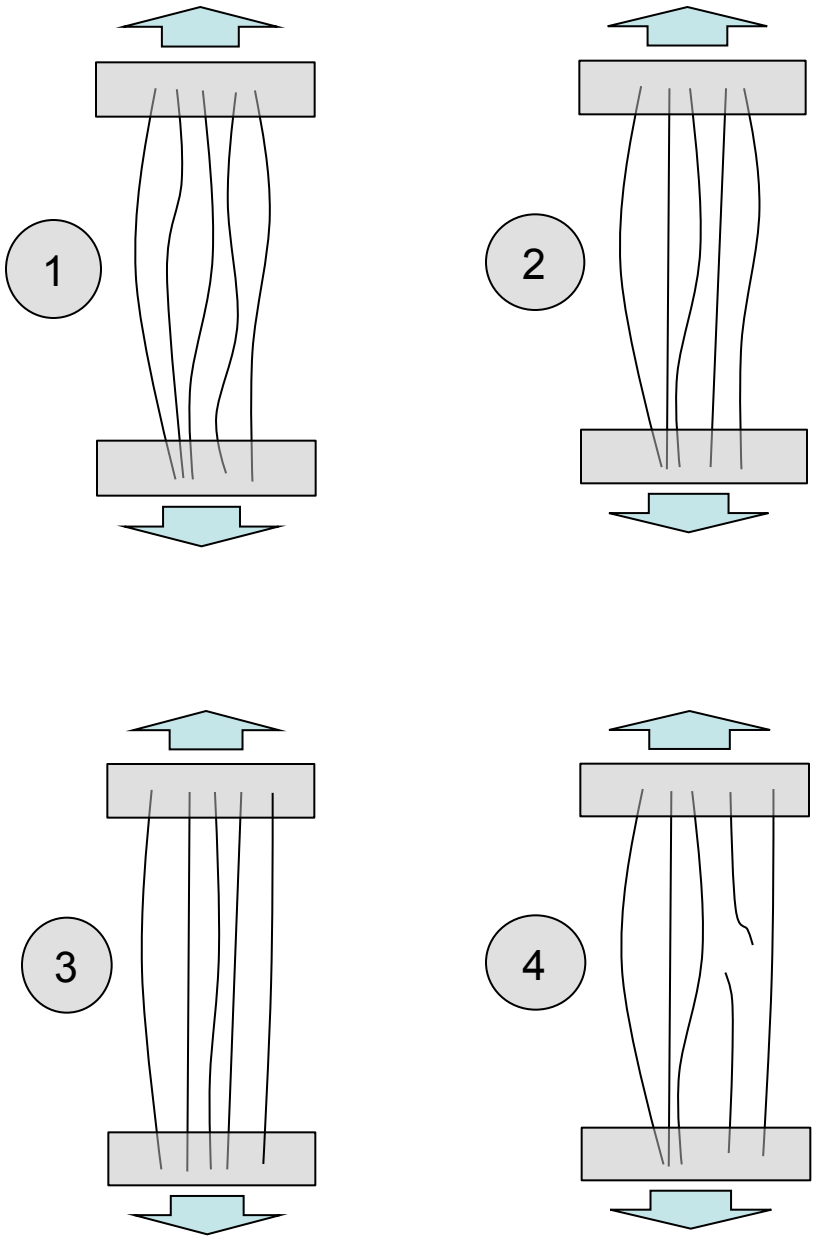

Figure 3.3 (b): carbon fibers are gradually aligned as the tow is stretched, but uniform strain cannot applied to individual fibers.

following triangular function with respect to time, and the resulting current is measured. It is known that current peaks appear in both cathodic and anodic scan direction when an electrochemically reversible system is considered (Figure 3.5).

Fabricated batteries were galvanostatically cycled once with a current, C/30 or 0.184 mA between 0.01 and 1.5 V for a formation cycle. A formation cycle is first few cycles during which organic electrolytes decompose and solid-electrolyte interphase forms. Since charges consumed during this process are irreversible, this cycle should precede any measurement of interest. Cyclic voltammetry (CV) was then employed to obtain diffusion coefficients of lithium ions in carbon fibers with voltage scan rate from 0.1 to 3.2 mV/s between 0.01 and 1.5 V. Since fibers have a circular cross section, the diffusion equation was formulated in a cylindrical coordinate system as

$$\frac{\partial C}{\partial t} = D\left[\frac{\partial^2 C}{\partial r^2} + \frac{1}{r}\left(\frac{\partial C}{\partial r}\right)\right], \tag{1}$$

where C is the concentration, r is the radius of a single filament, and t is the time. The boundary condition that the net flux of diffusing species at the electrode surface is equal to zero can be expressed as

$$D_O\left(\frac{\partial C_O(r,t)}{\partial r}\right)_a + D_R\left(\frac{\partial C_R(r,t)}{\partial r}\right)_a = 0 \tag{2}$$

where D's are the diffusion coefficients of oxidizing and reducing species, and a is the radius of a fiber.

In CV, the electric potential E can be expressed with the initial potential E_i and voltage scan rate v as

$$E = E_i + vt. \tag{3}$$

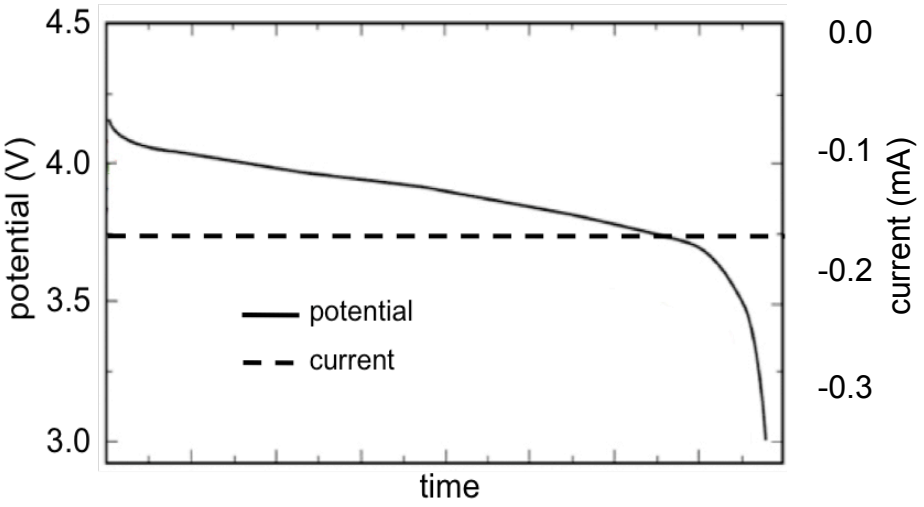

Figure 3.4: change in potential is measured while battery is discharged with a constantly imposed current in galvanostatic cycling.

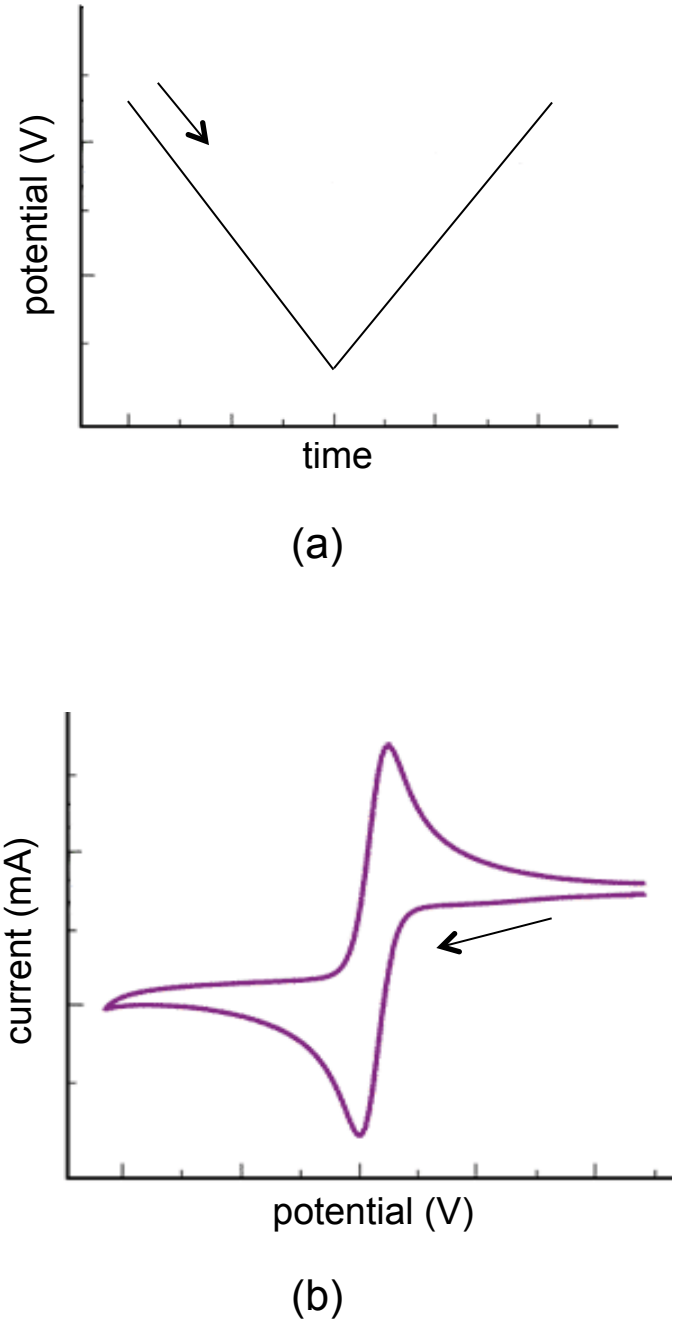

Figure 3.5: in cyclic voltammetry, (a) potential is controlled as a triangular function with various potential scan rates and (b) resulting current in a reversible system shows peaks in both scan directions.

Nernst equation combined with equation 3 gives

$$E_i + vt = E^0 + \frac{RT}{nF}\log\left[\frac{f_O C_O}{f_R C_R}\right], \tag{4-a}$$

$$\text{or} \quad \frac{C_O}{C_R} = \frac{f_R}{f_O}\exp\left[\frac{nF}{RT}\left(E_i - E^0\right)\right]\exp\left[\frac{nF}{RT}vt\right], \tag{4-b}$$

where R is the universal gas constant, T is the absolute temperature, n is the charge-transfer number, and F is the Faraday constant.

Nicholson solved these equations by a finite difference method [5]. From the following relationship between current i and concentration gradient,

$$i = nFAD\left(\frac{\partial C}{\partial r}\right)_a, \tag{5}$$

the current can be expressed as

$$i = \pm 1.475\frac{n^{3/2}F^{3/2}}{R^{1/2}T^{1/2}}AD^{1/2}C^0 v^{1/2}\psi, \tag{6}$$

where A is the electrode surface area and values of ψ are available from the references [5,6].

RESULTS AND DISCUSSION

One of the tensile test results of a battery is shown in Figure 3.3(a,b). As the fibers were stretched, the load stayed close to zero up to a certain point, here about 0.7 mm, where most fibers were straightened and started to be actually loaded, and then the load rapidly increased as more filaments were engaged in tension at about 0.90 mm. The tensile modulus of this sample was 360 GPa, which is about 38 % of the actual value, and

the ultimate elongation was 0.3 %, which is also smaller than the value provided by the manufacturer, indicating the applied load was not evenly distributed among filaments.

Figure 3.6 shows galvanostatic discharge/charge curves with a C/30 current. The initial voltage of a fresh battery was around 3.3 V and it dropped rapidly as the battery was discharged. The discharge curve became gentle from 1.8 V down to 0.4 V implying electrolyte DEC and EC decomposition [7]. Then the discharge curve plateaued at a few different potentials, referred as staging phenomena due to lithium ion intercalation into graphite (Figure 3.6 insets). The first discharge and charge capacities were 186 mAh/g and 162 mAh/g, respectively. These values correspond to 43~50% of theoretical capacity of graphite, 372 mAh/g. Limited graphite contents or degree of graphitization of the fiber are thought to be the major cause of the battery having lower utilization. It is well known that the capacity of carbon-based electrode is largely dependent on the graphitization degree [8-11]. Another reason of having lower utilization may be sought from the battery configuration. For the purpose of the experiment, compression between two electrodes could not be applied which is common procedure in conventional batteries. Finite distance between the two electrodes may cause the battery to have lower capacity owing to excessive concentration polarization.

Cyclic voltammetry with various scan rates ranging from 0.1 to 1.6 mV/s were conducted and the results of a control sample are shown in Figure 3.7. As the applied voltage scan rate increased, peak currents increased from 0.8945 to 1.613 mA and the position of anodic peak also shifted from 0.3706 to 0.6708 V. At very low potential scan rate, it is known that distinct peaks corresponding to different stages described with

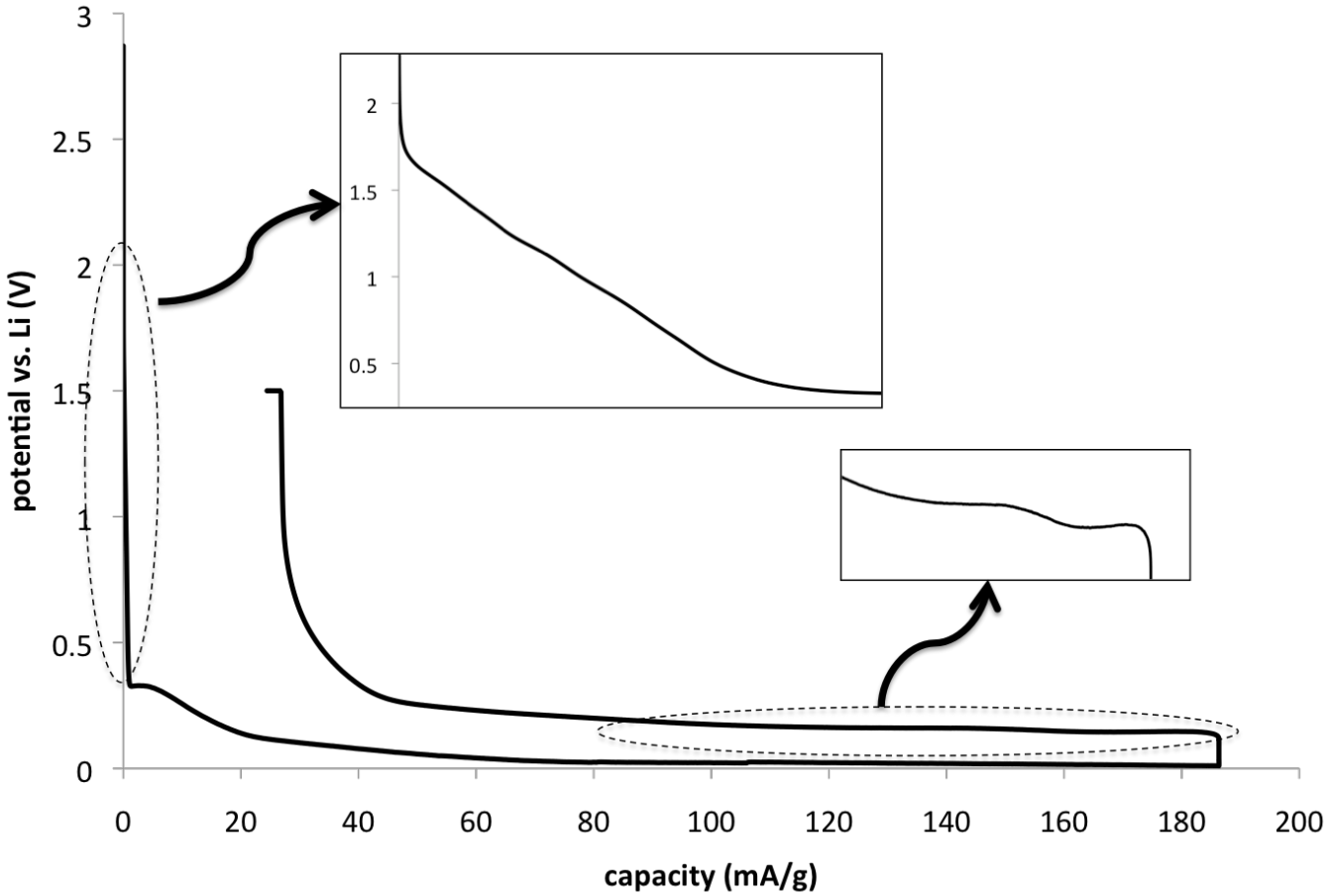

Figure 3.6: galvanostatic discharge/charge curve, (top inset) showing gentle curve due to electrolyte decomposition, (bottom inset) voltage plateau due to staging effects.

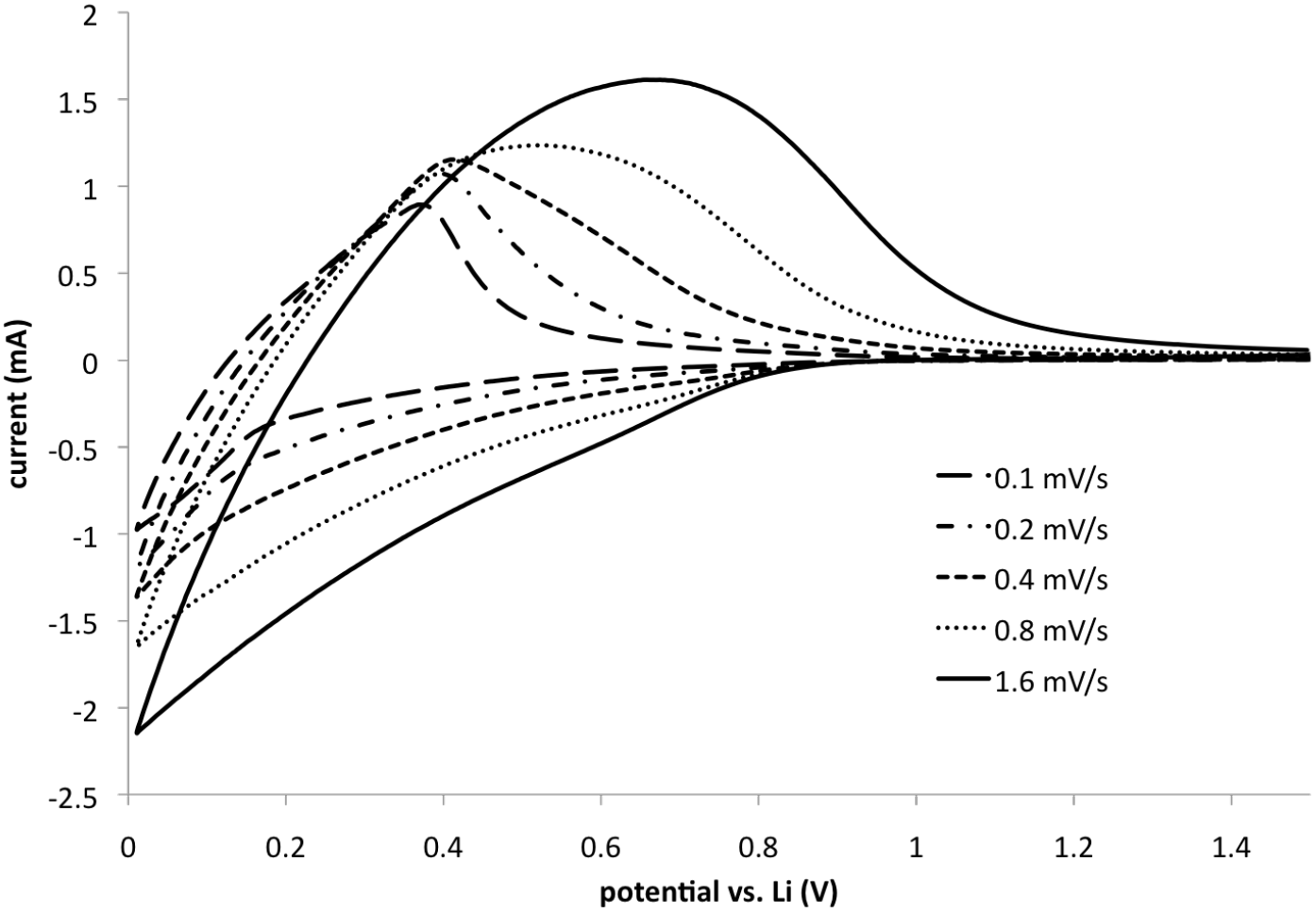

Figure 3.7: cyclic voltammogram with potential scan rates between 0.1 and 1.6 mV/s in a control sample.

galvanostatic charge-discharge appear in voltammogram (Figure 3.8), but they merge into one peak as scan rate increases [12].

From Equation 3.6, the peak current is the function of the diffusion coefficient and the square roots of potential scan rates. When the peak current is plotted against the square roots of the potential scan rates, the proportionality of these two values can be used to obtain a diffusion coefficient. From the result shown in Figure 3.7, the diffusion coefficient of lithium ions in the control carbon fibers was 3.1×10^{-6} cm^2/s using Equation 6.

Figure 3.9 presents a cyclic voltammogram with the fixed scan rate 0.1 mV/s and 0, 0.15, and 0.30 % of strains. The peak current increased from 0.5191 to 0.5583 to 0.6661 mA as the applied strain increased. Changes in peak position shifting from 0.3509 to 0.3596 to 0.3526 V were not as significant as the peak current changes with respect to scan rate variances. For a reversible system, increase of potential scan rates induces increase of peak currents while keeping the distance between cathodic and anodic peak positions constant. However, in a quasi-reversible system as in this study, potential scan rate affects both peak current and peak positions [13]. Given that the potential scan rate and peak position remained constant, we can deduce that the peak currents were increased by altered kinetic parameters, especially diffusivity.

In Figure 3.10, the peak currents from cyclic voltammogram of a sample under different tensions are plotted against the square roots of potential scan rates, and interpolated with linear functions. The slopes of these regression lines vary from 0.35 to 0.61 $mA/(mV/s)^{1/2}$ and diffusion coefficients corresponding to these slopes can be obtained in the range, 8.06×10^{-7} ~2.4×10^{-6} cm^2/s. Though the slopes in Figure 3.10 and in

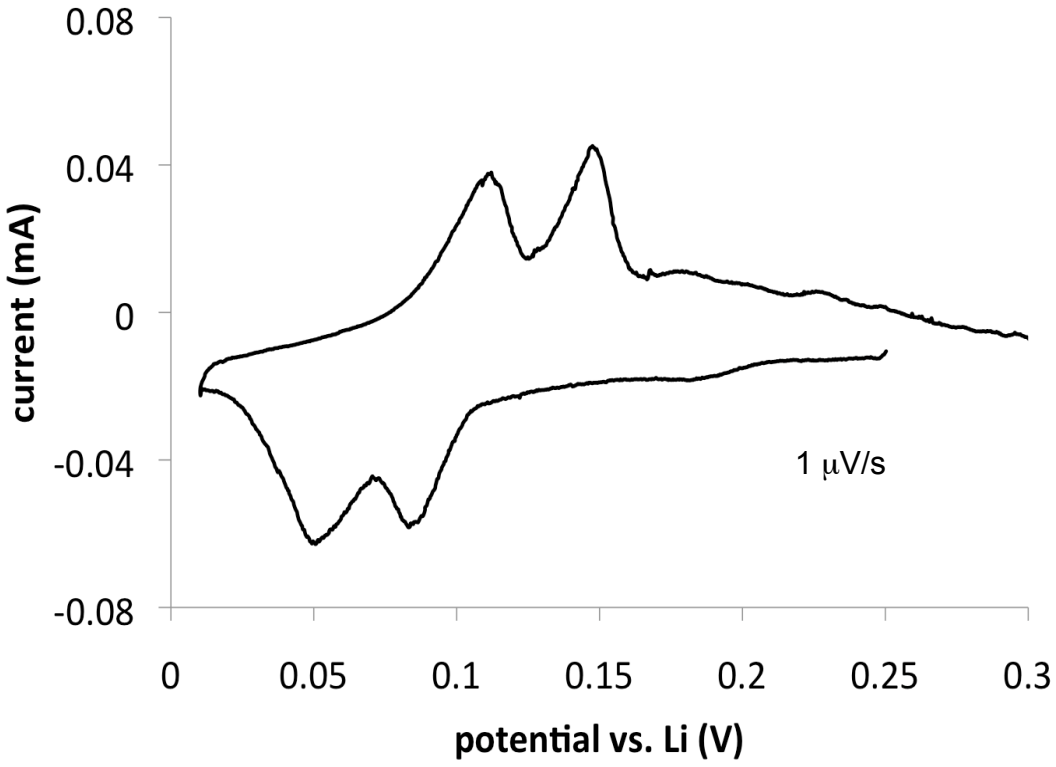

Figure 3.8: distinct current peaks appear when graphite is cycled with very low potential scan rate (1μV/s).

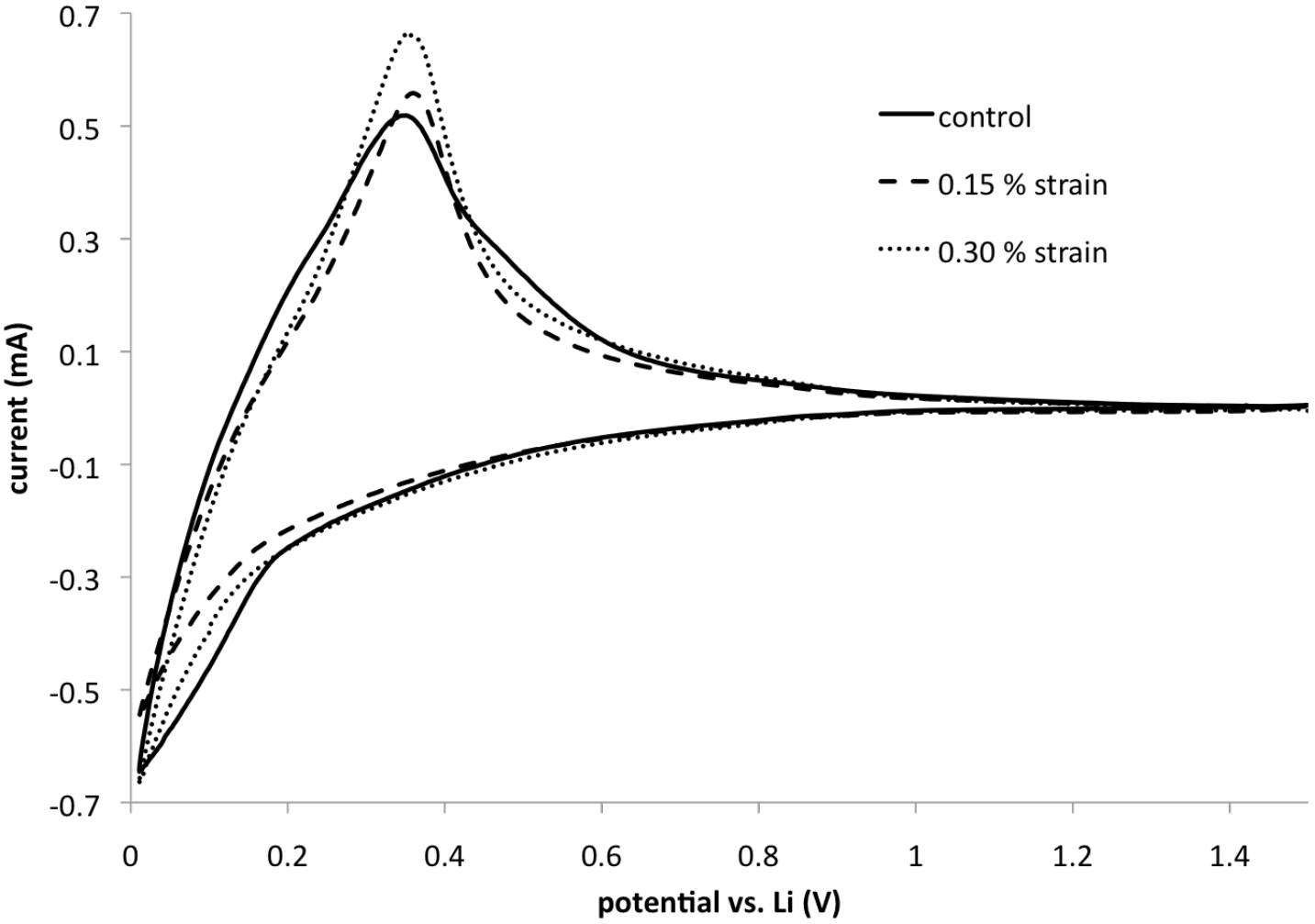

Figure 3.9: cyclic voltammogram with various strains.

other samples changed with respect to the applied strains, they did not seem to have a statistically meaningful trend among various samples as shown in Figure 3.11.

The diffusion coefficients obtained from the experiments were in the same order with those Takami *et al.* reported using EIS [14], but 3 to 4 orders of magnitude larger compared to other studies measuring diffusivity of carbon fibers with various techniques [15-17]. Takami and co-workers explained that the high diffusivity of lithium ions in carbon fibers was attributed to the radial texture of filament microstructure. In literature, however, diffusivity of lithium ions in graphite is not in good agreement and various depending on physical and chemical characteristics of materials and electrochemical techniques used for the diffusivity measurement [18].

One reason that the diffusivity varies in strained carbon fibers may be the deformation of microstructures. Imanish *et al*. studied how the microstructure of a carbon fiber affects the capacity and cyclability [19]. They explained the dependence of battery functions on crystallite structure as the difference in susceptibility to structural failure and lithium ion accessibility. Shioya and Takaku [20] reported re-orientations of crystallites in carbon fibers under tension using X-ray diffraction. Therefore, the alteration of diffusion path due to rigid rotation of crystallites under tension might be an important cause of the change in diffusivities. Another possible cause came from the uncertainty of the tensile test. As seen in Figure 3.3, when fibers were stretched, individual fibers were subject to different strains from each other due to technical difficulty of alignment of multiple fibers. Consequently, the diffusion coefficient of tested battery was the averaged results obtained with differently strained fibers, in which the strain was an important control parameter.

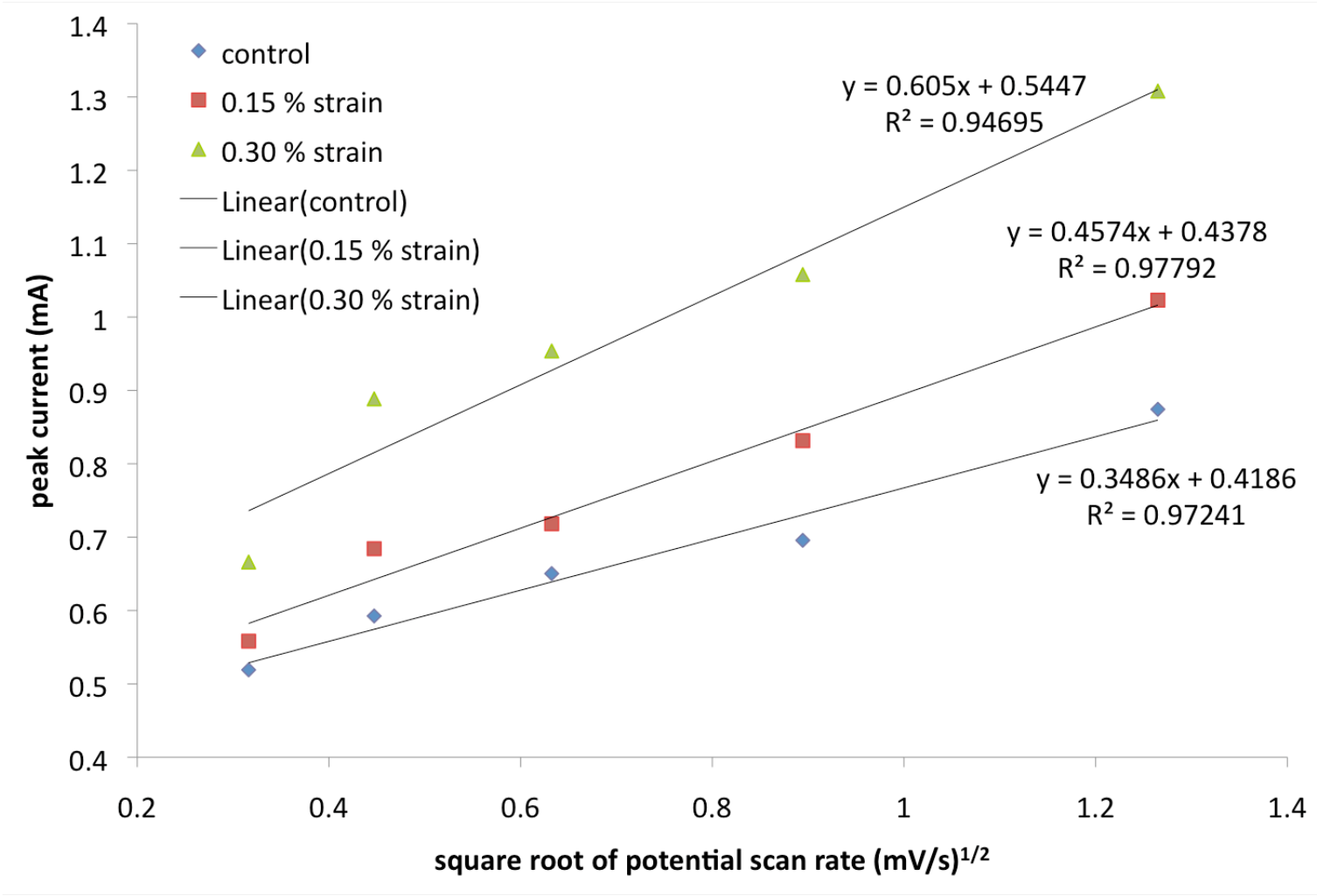

Figure 3.10: peak current vs. square root of potential scan rate. Regression lines are added to see changes in the relationship with respect to the applied loadings

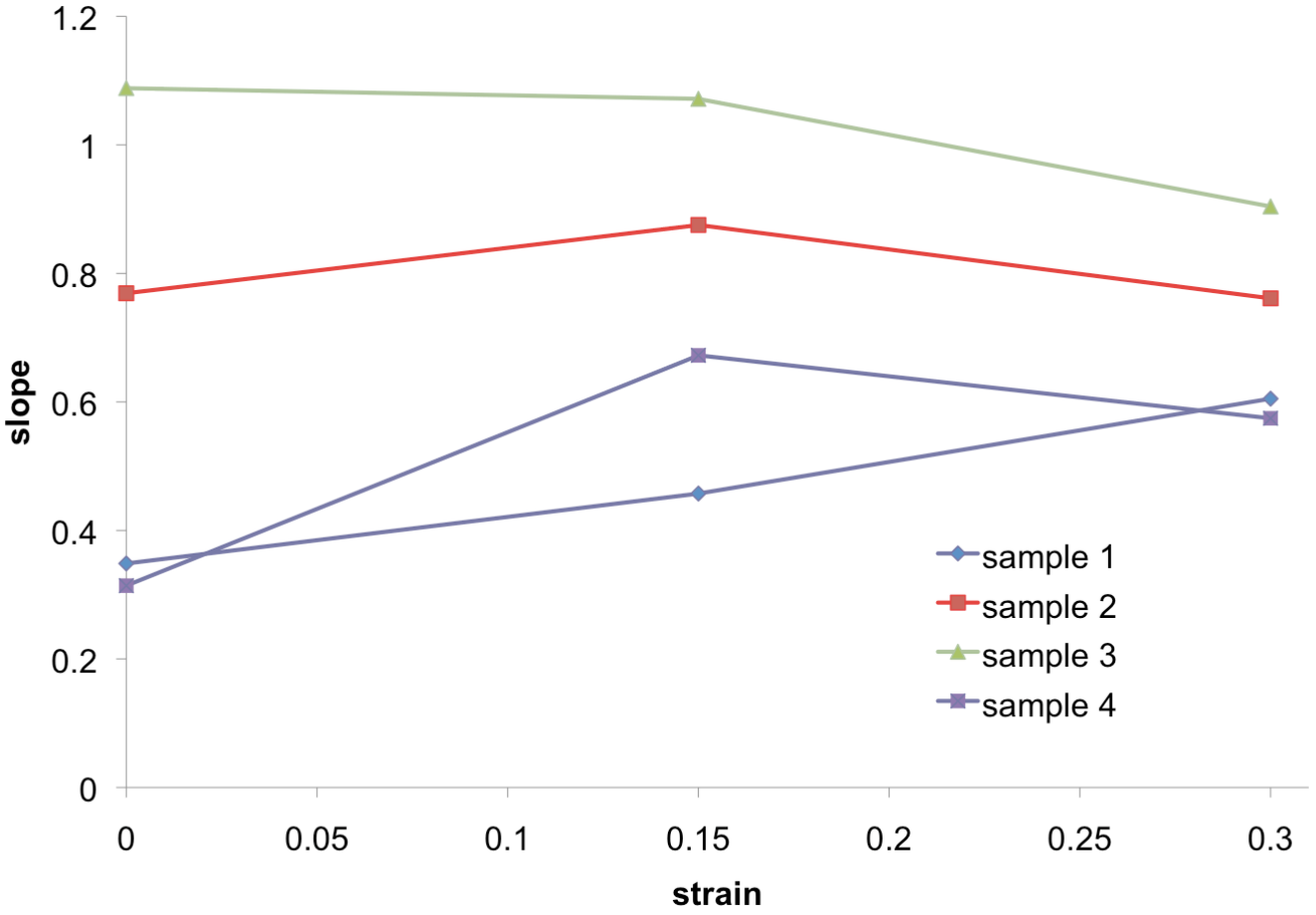

Figure 3.11: slopes from Figure 3.10 are plotted against strain. Slopes vary, but not in a significant pattern.

When strains were applied to a structural battery, and the battery was charged/discharged, the battery experienced change in stresses. As seen in Figure 3.12, the load measured with the materials tester decreased from 55 down to 44 N during discharging and recovered the initial loading at the completion of one full electrochemical cycle. The pattern of the measured load was precisely consistent with that of charges (Figure 3.12), and the magnitude of change in load during cycling was also directly proportional to the amount of charges (Figure 3.13), implying the number of lithium ions inserted into graphite was a key factor.

Previous experimental work using X-ray [15,21,22] and computational work [23] showed that graphite lattices expand as lithium ions intercalate into graphite and agreed that the change in spacing between lattices was less than 10 %. Thus, we can deduce that the measured load change up to 20 % originated not only from the elongated lattices, but also more likely from other factors in the carbon fiber due to lithium intercalation. In carbon fibers, the graphite lattices are aligned along fiber direction. In other words, the c-axis of graphite is perpendicular to the fiber to have higher stiffness and strength although all the graphite lattices are not perfectly aligned within a fiber [24]. This fact strengthens the postulation that the changes in the measured load shown in Figure 3.12 and 3.13 are more likely intrinsic.

Considering design of structural batteries or battery-implemented applications, the findings in this experimental study may be used as a criterion. Since the intrinsic property of an active material significantly changes during battery operation, one cannot adopt materials properties reported for uses in typical structural applications. Instead, significantly conservative design criteria should be applied. Changes in battery functions,

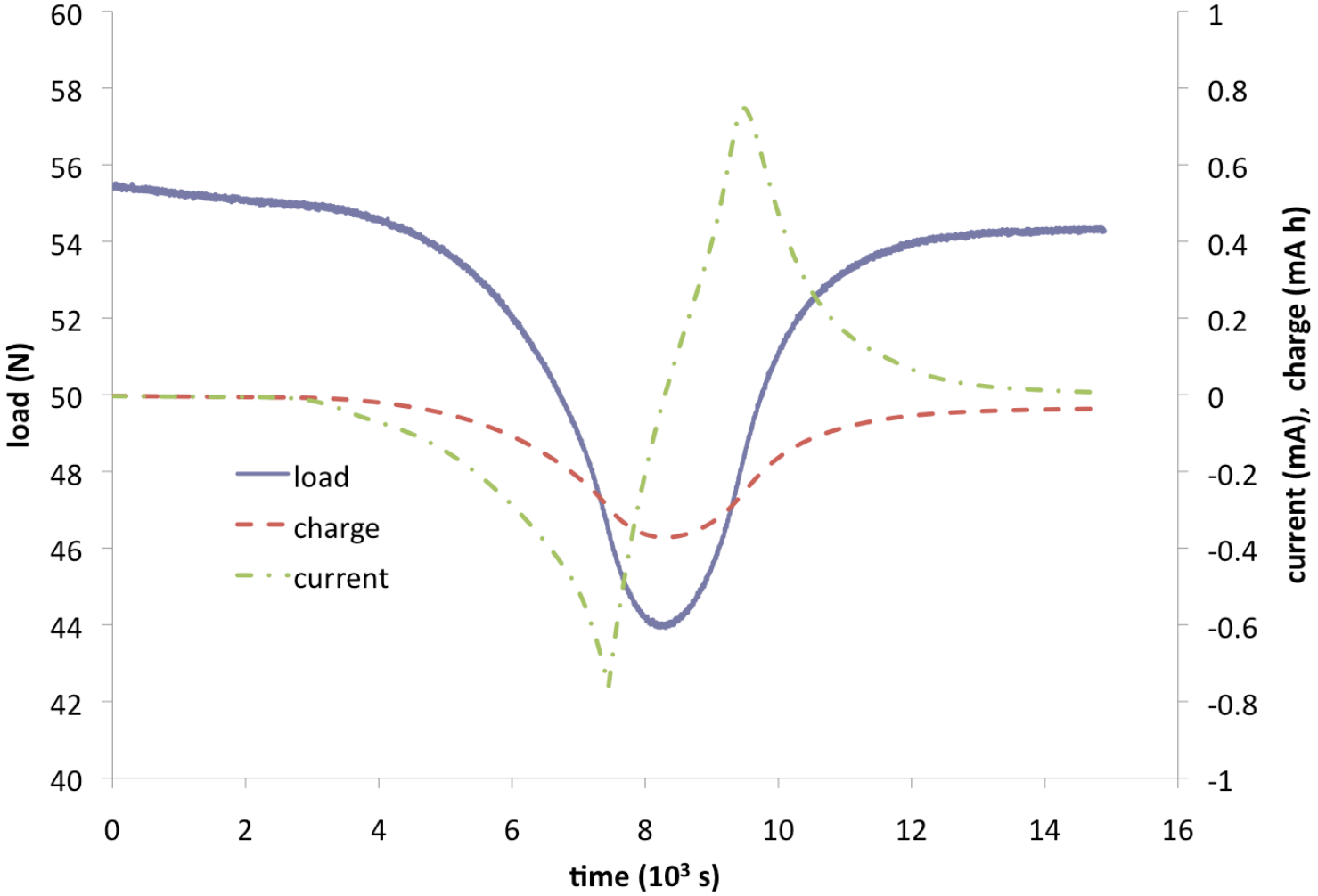

Figure 3.12: measured load changes as lithium ions intercalate into graphite as shown with the charge and current curves.

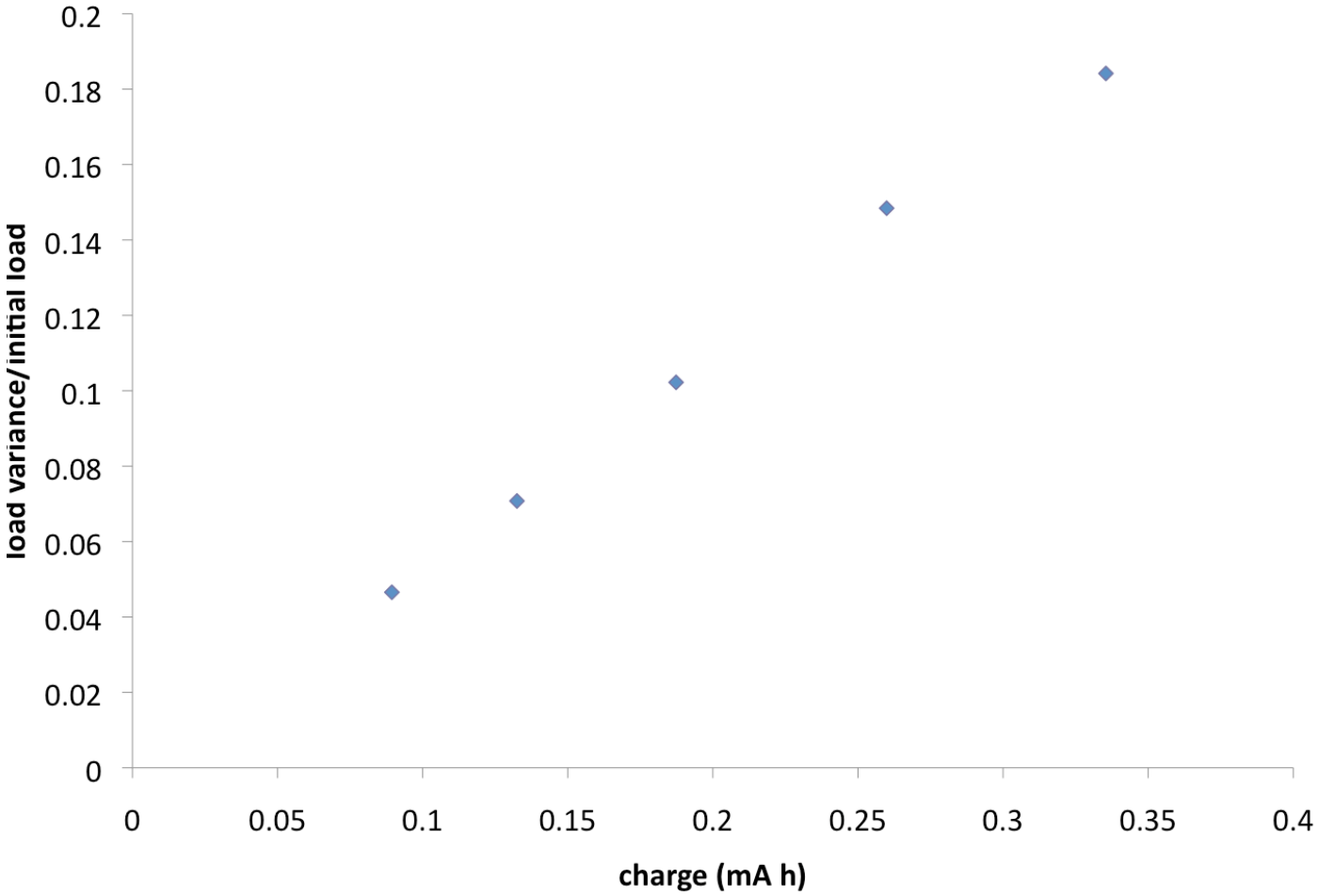

Figure 3.13: change in measured loads is directly proportional to the amount of lithium ions inserted into graphite .

though they were not as significant as structural aspects from this study, should also be carefully considered.

As the final thought on the experiment, differently from porous materials, tensions applied to the fibers may not cause the fibers to contract laterally as a whole so that individual filaments can better contact to each other. This is because there is no structural connection between individual fibers. Even though the contact between fibers may slightly differ from relaxed fibers to strained ones, the electronic conduction in carbon fibers mainly occur along the longitudinal direction due to high anisotropy of graphite. This reasoning made the assumption feasible that we alter the actual material differently from previous work using porous materials.

CONCLUSIONS AND FUTURE WORK

In this study, we studied the effects of mechanical stresses on electrochemical performance of batteries. A carbon fiber - lithium battery was fabricated for a coupled mechanical-electrochemical experiments. The diffusion coefficients of lithium ions in carbon fiber were measured using CV and the load applied to the fiber was monitored while the carbon fiber (working electrode) was stretched with a material tester. The diffusivity obtained from experiments under strains of 0 ~ 0.3% varied from 8.06×10^{-7} to 2.4×10^{-6} cm^2/s within the same sample. The change in lithium ion diffusivity may be caused by alteration of diffusion path due to microstructure changes during tension tests, but did not result a statistically meaningful trend. Load measured during electrochemical cycling strongly depended on the amount of lithium ions intercalated into graphite. Considering findings from previous work and arrangement of graphite lattices, the

changes in measured loadings may be caused by materials property change rather than expansion of the material. It is recommended that this possibility of material property change should be considered when designing a structural battery.

To better understand the underlying mechanism in the change of diffusivity under external mechanical stresses, characterization of the carbon fiber microstructure would be required. Observation of lattice parameter and orientation change of the carbon fiber using X-ray during tension tests may clarify the direct cause of change in diffusivity.

One of the difficulties in this study was to make filaments evenly align with the loading so that every single filament is under the same strain. We can resolve this problem by testing a single filament instead of a tow of fibers. However, designing a battery that can be used in this type of coupled experiments is not trivial, considering grabbing a brittle fiber for tension tests and sealing the battery while allowing motion for material tests.

BIBLIOGRAPHY

24. Striebel, K.A., Sierra, A., Shim, J., Wang, C.-W., and Sastry, A.M., 2004, "The effect of compression on natural graphite anode performance and matrix conductivity," Journal of Power Sources, v.134, pp.241-251.

25. Wang, C.-W., Yi, Y.-B., Sastry, A.M., Shim, J. and Striebel, K.A., 2004, "Particle Compression and Conductivity in Li-ion Anodes with Graphite Additives," Journal of the Electrochemical Society, v. 151 (9), pp. 1489-1498.

26. Yi, Y.-B., Wang, C.-W. and Sastry, A.M., 2006, "Compression of Packed Particulate Systems: Simulations and Experiments in Graphitic Li-ion Anodes," ASME Journal of Engineering Materials and Technology, v. 128(1), pp. 73-80.

27. Choi, Y.-M., and Pyun, S.-I., 1997, "Effects of intercalation-induced stress on lithium transport through porous $LiCoO_2$ electrod," Solid State Ionics, v.99, pp.173-183.

28. Nicholson, M.M., 1954, "Diffusion Currents at Cylindrical Electrodes. A Study of Organic Sulfides," Journal of the American Chemical Society, v.76, pp.2539-2545.

29. Delahay, P., 1954, New Instrumental Methods in Electrochemistry, p.121, Interscience Publishers, Inc., New York.

30. Choi, Y.-K., Chung, K.-I., Kim, W.-S. and Sung, Y.-E., 2001, "Electrochemical properties of passivation film on mesophase pitch-based carbon fiber electrode," Microchemical Journal, v.68, pp.61-70.

31. Iijima, T., Suzuki, K. and Matsuda, Y., 1995, "Electrodic characteristics of various carbon materials for lithium rechargeable batteries," Synthetic Metals, V.73, pp.9-20.

32. Ohsaki, T., Kanda, M., Aoki, Y., Shiroki, H., and Suzuki, S., 1997, "High-capacity lithium-ion cells using graphitized mesophase-pitch-based carbon fiber anodes," Journal of Power Sources, v.68, pp.102-105.

33. Flandrois, S. and Simon, B., 1999, "Carbon materials for lithium-ion rechargeable batteries," Carbon, v.37, pp.165-180.

34. Kinoshita, K. and Zaghib, K., 2002, "Negative electrodes for Li-ion batteries," Journal of Power Sources, v.110, pp.416-423.

35. Kulova, T.L. and Skundin, A.M., 2006, "Balance between Reversible and Irreversible Processes during Lithium Intercalation in Graphite," Russian Journal of Electrochemistry, v.42, pp.251-258.

36. Bard, A.J. and Faulkner, L.R., *Electrochemical Methods, Fundamentals and Applications*, p.239, John Wiley & Sons, Inc., Hoboken, NJ (2001).

37. Takami, N., Satoh, A., Hara, M. and Ohsaki, T., 1995, "Structural and Kinetic Characterization of Lithium Intercation into Carbon Anodes for Secondary Lithium Batteries," Journal of the Electrochemimcal Society, v.142, pp.371-379.

38. Uchida, T., Morikawa, Y., Ikuta, H., and Wakihara, M., 1996, "Chemical Diffusion Coefficient of Lithium in Carbon Fiber," Journal of the Electrochemical Society, v.143, pp.2606-2610.

39. Morita, M., Nishimura, N.and Matsuda, Y., 1993, "Charge/Discharge Cycling Behavior of Pitch-based Carbon Fiber in Organic Electrolyte Solution," Electrochimica Acta, v.38, pp.1721-1726

40. Verbrugge, M.W. and Koch, B.J., 1996, "Modeling Lithium Intercalation of Single-Fiber Carbon Microelectrodes," Journal of The Electrochemical Society, v.143, pp.600-608.

41. Yu, P., Popov, B.N., Ritter, J.A. and White, R.E., 1999, "Determination of the Lithium Ion Diffusion Coefficient in Graphite," Journal of the Electrochemical Society, v.146, pp.8-14.

42. Imanishi, N., Kashiwagi, H., Ichikawa, T., Takeda, Y. and Yamamoto, O., 1993, "Charge-Discharge Characteristics of Mesophase-Pitch-Based Carbon Fibers for Lithium Cells," Journal of the Electrochemical Society, v.140, pp.315-320.

43. Shioya, M. and Takaku, A., 1994, "Rotation and Extension of Crystallites in Carbon Fibers by Tensile Stress," Carbon, v.32, pp.615-619.

44. Skundin, A.M., Grigoreva, O.Y., Kulova, T.L., and Pouchko, S.V., 2003, "The lithium intercalation into graphite from electrolyte and from solid lithium," Journal of Solid State Electrochemistry, v.8, pp.11-14.

45. Hahn, M., Buqa, H., Ruch, P.W., Goers, D., Spahr, M.E., Ufheil, J., Novak, P., and Kotz, R., 2008, "A Dilatometric Study of Lithium Intercalation into Powder-Type Graphite Electrodes," Electrochemical and Solid-State Letters, v.11, pp.A151-A154.

46. Marquez, A., and Balbuena, P.B., 2001, "Molecular Dynamics Study of Graphite/Electrolyte Interafaces," Journal of the Electrochemical Society, v.148, pp.A624-A635.

47. Chung, D., Carbon Fiber Composites, Butterworth-Heinemann, Newton, MA.

CHAPTER IV

MOLECULAR DYNAMICS SIMULATION OF LITHIUM ION DIFFUSION IN GRAPHITE UNDER MECHANICAL STRESSES[3]

INTRODUCTION

There are multiple sources of mechanical stresses exerted on batteries during their fabrication and operation. Compression is a typical process to compact porous materials and to decrease contact resistance within active materials and between active materials and current collectors. While batteries are in operation, they experience cyclic loadings from chemical reactions such as lithium intercalation into host materials and thermal expansion and contraction. These mechanical stresses have been blamed for the mechanical failure of active materials, and consequently the failure of batteries due to loss of conduction path. Moreover, these mechanical stresses may also affect the functionality of battery while they are in operation such as capacity, cyclability, and rapid charge-discharge capability.

Molecular dynamics (MD) simulation is a method that enables us to directly understand how each species of interest behaves at an atomic level. This method has been adopted in simulating battery system for the last two decade. Using Monte Carlo

[3] Material in this chapter is an unpublished paper in progress: H. C. Kim and A. M. Sastry, Molecular Dynamics Simulation of Lithium Ion Diffusion in Graphite under Mechanical Stresses, *Journal of the Electrochemical Society*, (2009).

simulation, Lehnert and Schmickler investigated the diffusion of lithium atoms in graphite lattice and found that lithium atoms are ionized by donating their valence electron to the host material, lithium ions diffuse parallel to graphite planes rather than across planes due to energy barrier difference and the ions diffuse by thermal activation [1]. Shimizu and Tachikawa compared the migration process of lithium atoms and ions using molecular dynamics simulation, and found that lithium ions form ionic bonding with carbon atoms, but lithium atoms covalently bond with carbons [2]. Marquez *et al*. conducted molecular dynamics simulations of reactions at graphite/electrolyte interfaces and they evaluated staging phenomena, structural change in graphite, charge distribution on the atoms, and lithium ion diffusion coefficient as a function of lithium concentration in graphite [3].

On the other hand, MD has been intensively applied to understand mechanics of carbon nanotube (CNT). Mechanical properties such as Young's modulus, Poisson's ratio, and tensile strength were calculated using the multi-body potential function of embedded atom method [4], the modified Morse potential [5], and the Brenner potential [6]. The tensile and compressive properties of bundles of CNTs were also measured with Brenner potential and Lennard-Jones potential together [7]. Fracture of CNTs was also investigated using MD [8,9].

As listed above, applications of MD to structural and electrochemical analyses have been separately made. However, considering the detrimental effects of mechanical stresses to battery performances and lifetime, it is worth to investigate the relation between stresses and battery functions. MD seems to be the best approach to this problem

since it can be conveniently done to quantify specific values such as stresses and diffusivities.

In this article, thus, we analyzed the effects of mechanical stresses on lithium ion battery functions using molecular dynamics simulation with the Brenner potential widely used for modeling of graphite and diamond. Our specific objectives are as follows:

1. To measure the difference in lithium ion diffusivities in graphite when it is relaxed and stressed.
2. To observe changes in lattice parameters and stresses due to lithium intercalation.
3. To quantify material properties of graphite and lithium intercalated graphite.

METHODS

MD simulations of lithium-ion diffusion in graphite lattices were performed with a canonical ensemble or NVT where the number of particles N, the volume V, and the temperature T were kept constant. Lithium ions were placed between 4 lattices of graphite each containing 88 carbon atoms. The Verlet algorithm was used for integration, and velocity rescaling was used for adjustment of temperature to 300 K. The time step used for the simulation was 0.5 fs and the total running time was 5 ps. Ion diffusivity was calculated with different boundary conditions to evaluate the mechanical stress effects.

POTENTIAL FUNCTIONS

The Brenner potential is a bond-order empirical potential which describes the covalent bonding energy, E_{bond} in hydrocarbon molecules, graphite and diamond [10]. The potential is expressed as the difference of a repulsion term V_R and an attraction term V_A modified with b^*,

$$E_{bond} = V_R(r) - b^* V_A(r) . \tag{1}$$

The term b^* is the bond order which depends on the number of bonds or types of sp hybridization in carbon-containing molecules. The repulsion and attraction terms are expressed as exponential functions as

$$V_R(r) = f_c(r)\frac{D_e}{S-1}\exp\left\{-\beta\sqrt{2S}\left(r - R_e\right)\right\}, \tag{2a}$$

$$\text{and} \quad V_A(r) = f_c(r)\frac{D_e S}{S-1}\exp\left\{-\beta\sqrt{2/S}\left(r - R_e\right)\right\}, \tag{2b}$$

where D_e is the potential well depth, R_e is the equilibrium constant, and f_c is the cut-off function which thins between R_1 and R_2 expressed as

$$\text{and} \quad f_c(r) = \begin{cases} 1 & r < R_1 \\ \left\{1 + \cos\left[\dfrac{\pi(r - R_1)}{R_2 - R_1}\right]\right\}/2 & R_1 < r < R_2 \\ 0 & r > R_2 \end{cases} . \tag{3}$$

As explained above, the term b^* incorporate the bond order by taking the bond angles into account among the atoms i, j, and k as in the following equation and in Figure 4.1.

$$b^* = \frac{b_{ij} + b_{ij}}{2},\ b_{ij} = \left(1 + a\left\{\sum_{k \neq i,j} f_c(r_{ik}) g\left(\theta_{ijk}\right)\right\}^n\right)^{-\delta} \tag{4}$$

where $g\left(\theta_{ijk}\right) = 1 + \dfrac{c^2}{d^2} - \dfrac{c^2}{d^2 + \left(h - \cos\theta\right)^2}$. All the parameters used with Brenner potential are listed in Table 4.1.

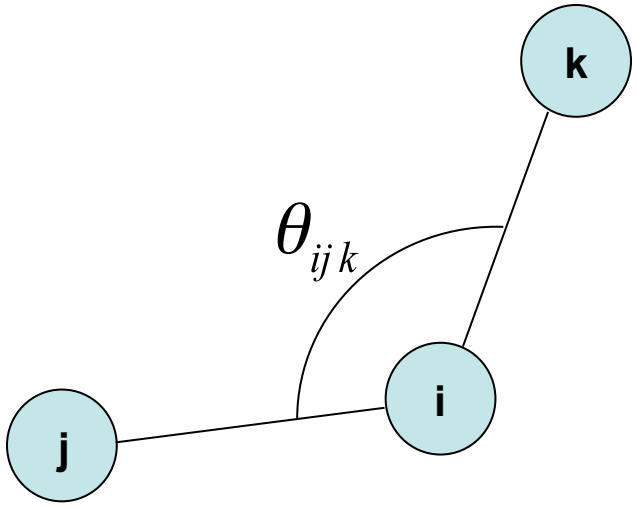

Figure 4.1: inter atomic angle configuration among atoms i, j, and k

D_e(eV)	R_e(Å)	β (Å^{-1})	R_1(Å)	R_2(Å)	S
6.325	1.315	1.5	1.7	2.0	1.29
a	n	c	d	h	δ
0.0011304	1	19	2.5	-1	0.80469

Table 4.1: Parameters for Brenner Potential.

Non-bonding potentials consist of Lennard-Jones potential E_{vdW} and Coulomb potential $E_{Coulomb}$. These potentials describe the interactions between graphite lattices and the interaction between lithium ions and graphite as

$$E_{vdW} = D_{ij}\left\{\left(\frac{\sigma_{ij}}{r_{ij}}\right)^{12} - 2\left(\frac{\sigma_{ij}}{r_{ij}}\right)^{6}\right\}, \tag{5}$$

$$\text{and } E_{Coulomb} = C_0\left(\frac{Q_i Q_j}{r_{ij}}\right), \tag{6}$$

where D_{ij} is the potential well depth, and σ_{ij} is the equilibrium length, C_0 is the Coulomb constant, and Q_i is the electric charge associated with i^{th} atom. The parameters used for the non-bonding potentials are listed in Table 4.2.

The net charge in lithium ion intercalated graphite is zero since the number of lithium ions is equivalent to that of electrons transferred through electric circuit. These electrons are evenly distributed in the graphene layer due to the delocalized unoccupied molecular orbital of graphite. Thus, the charge δ each carbon atom contains is equal to 1/6 of that each lithium ion has in the stage 1 as in the following equation,

$$6\text{C} + \text{Li}^{+} + \text{e}^{-} \leftrightarrow \text{Li}^{\delta+}\text{C}_6^{\delta-}. \tag{7}$$

Song and co-workers calculated the charges in lithium intercalated graphite at various stages using local density functional approximation [11]. We adopted these values, *e.g.* $\delta_{Li} = 0.68$ in stage 1, for the simulations in this study.

SIMULATIONS AND MEASUREMENT

Simulations were performed to mimic uni-axial tension tests. All the boundary atoms on edge planes were fixed for control simulations and either edge or basal planes

D_C(kcal/mol)	0.1050
D_{Li}(kcal/mol)	0.0250
σ_C(Å)	3.8510
σ_{Li}(Å)	2.4510

Table 4.2: Parameters for Lennard-Jones Potential.

of the graphite lattices were stretched by the prescribed strain 1% of the dimension under consideration for tension test simulations. When tensions were applied, reaction forces exerted on the boundaries were measured.

While tension tests were conducted, diffusivity of a lithium ion D was calculated using time-dependent square displacement (TSD) method. TSD type diffusion coefficient can be expressed as

$$D = \frac{\sum_{i=1}^{\text{step}} (r_i - r_{i-1})^2}{6t}, \tag{8}$$

where r_i is the position of the ion at step i, and t is the total simulation time. Diffusion coefficients were measured at the stage 1 as shown in Figure 4.2.

RESULTS AND DISCUSSION

The diffusion coefficient of lithium ions in graphite was measured as (6.30 ± 0.08) × 10^{-7} cm^2/s at the room temperature. This value lies close to 9.0×10^{-7} cm^2/s which was obtained with a semi-empirical method, AM1 [12], but one or two orders larger than 1.0×10^{-9} ~ 2.1×10^{-8} cm^2/s calculated with the universal force field [3]. The diffusivities obtained with atomistic computer simulation are relatively in good agreement since most experimental results of lithium diffusivity include pore diffusion and also depend on material preparation, resulting large range of diffusivities from 5.0×10^{-11} to 1.0×10^{-7} cm^2/s as Marquez and Balbuena discussed [3].

Diffusivity of lithium ions appeared to significantly vary depending on whether graphite was strained or not (Figure 4.3). Diffusivities were measured as (6.50 ± 0.03) × 10^{-7} cm^2/s when 1 % strain was applied in the perpendicular direction to graphene

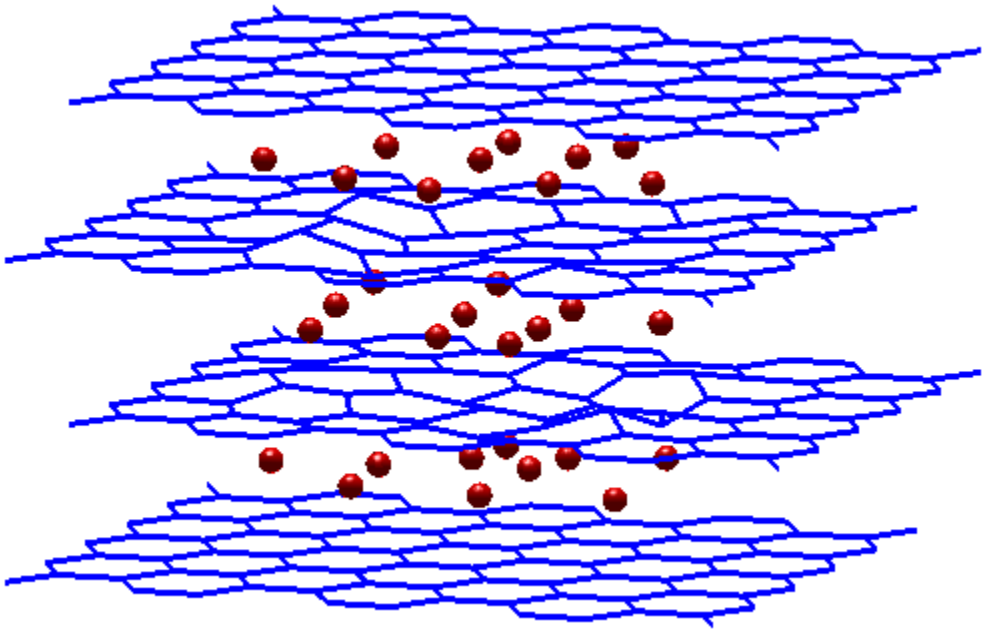

Figure 4.2: visualization of lithium intercalated graphite at stage 1.

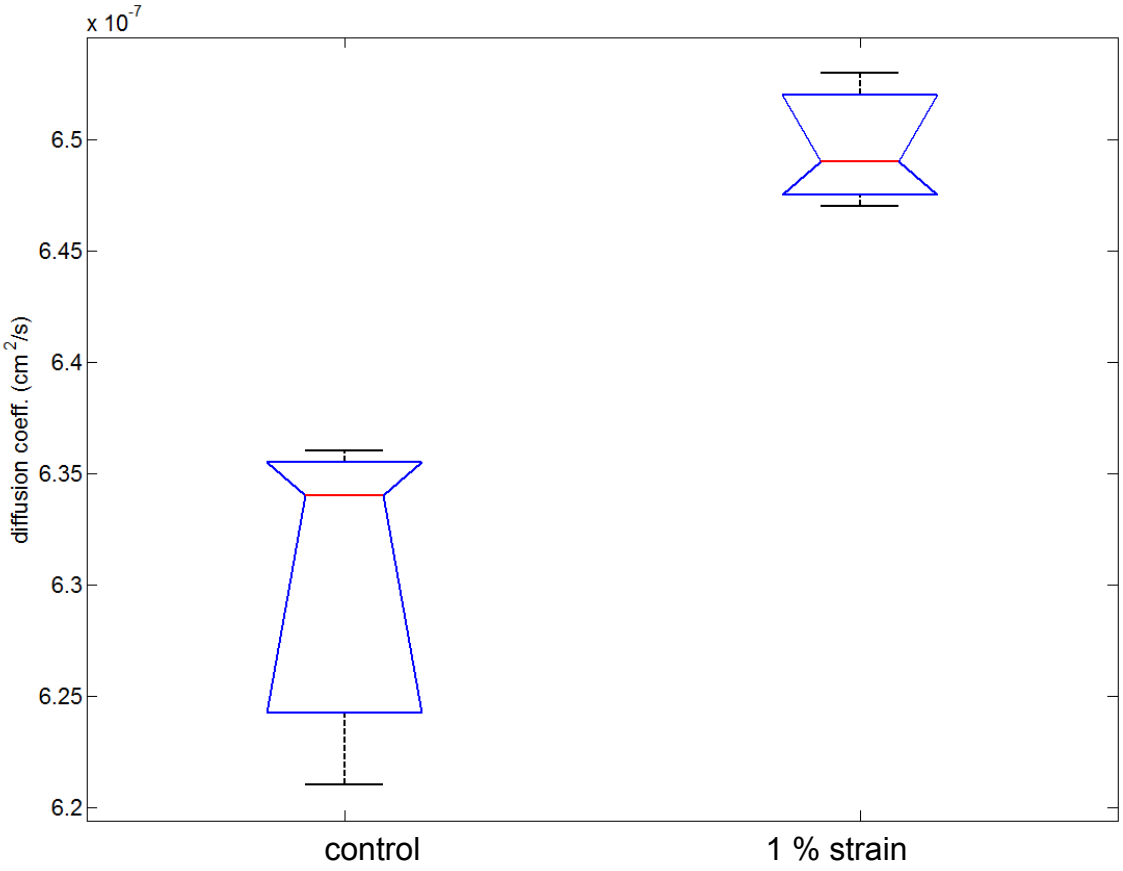

Figure 4.3: diffusion coefficient of lithium ions in graphite (left) no strain was applied to graphite (right) graphite was stretched by 1% in the perpendicular direction of graphene lattice

lattices, and this value is about 3 % larger than that in relaxed graphite. Since lithium ions diffuse by thermal vibrations which overcomes potential energy barrier [1], larger spacing, i.e. less energy barrier, may allow lithium ions to move more easily, resulting a larger diffusivity.

Figure 4.4 shows spacing between lattices increased from the initial value 3.35 Å to 3.385 Å due to lithium ion intercalation. Expansion of lattice spacing had been previously studied using X-ray during electrochemical cycling of lithium ion batteries [13-15]. Figure 4.5 shows the stress-strain curve of graphite where graphite was stretched in the perpendicular direction of graphene lattices. The elastic modulus in this direction was obtained as about 180 GPa, and that of lithium intercalated graphite was about 400 GPa, more than twice of pristine graphite. This is probably because carbon atoms in lithium intercalated graphite are more strongly constrained by Coulombic force with lithium ions.

CONCLUSIONS AND FUTURE WORK

Molecular dynamics simulation was conducted to evaluate the effects of mechanical stresses on battery function. Diffusion coefficients were measured with two different strain conditions and change in diffusion coefficients was found. Diffusivity of lithium ions in graphite was increased by 3% when graphite was strained 1% in the perpendicular direction to graphite lattices. Intercalated lithium caused the graphite lattice spacing to expand by 1%. Despite of the widened distance among carbon atoms, elastic modulus in perpendicular direction to lattices was increased due to attractive interactions with lithium ions.

As mentioned earlier, diffusivity in real battery always has larger variance than in computer model since the real system depends largely on material preparation and other limiting factors. It is important to consider other factors in analyses because diffusion processes are dominated by the slowest one. Thus, it is recommended to examine diffusions in the interface between graphite and electrolyte or solid-electrolyte interphase itself.

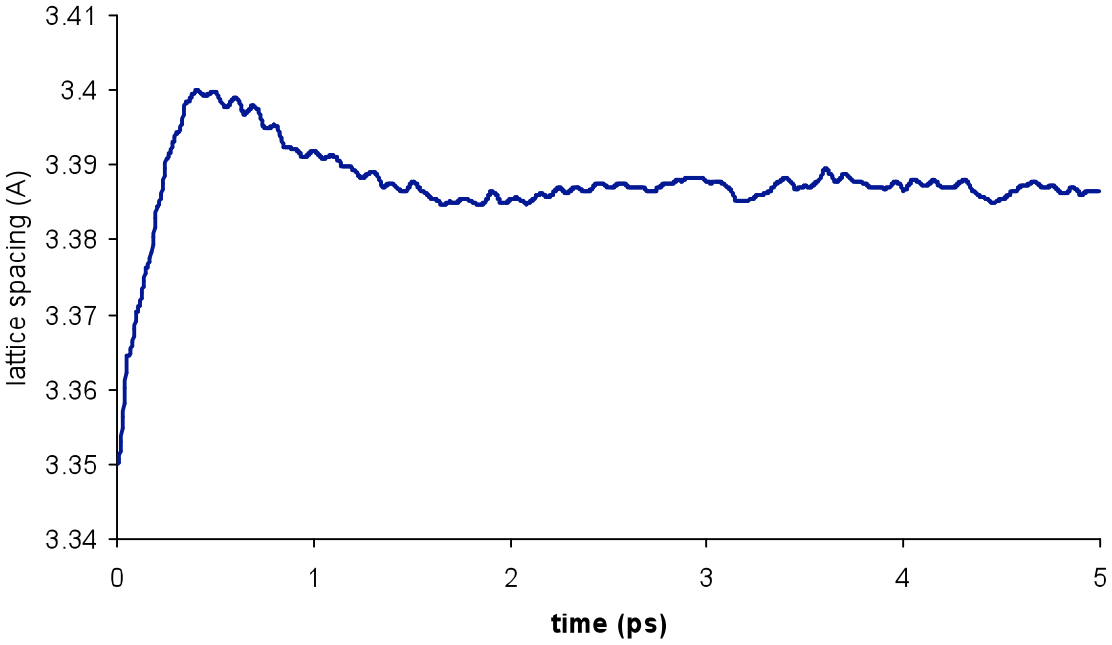

Figure 4.4: graphite lattice spacing during stage 1

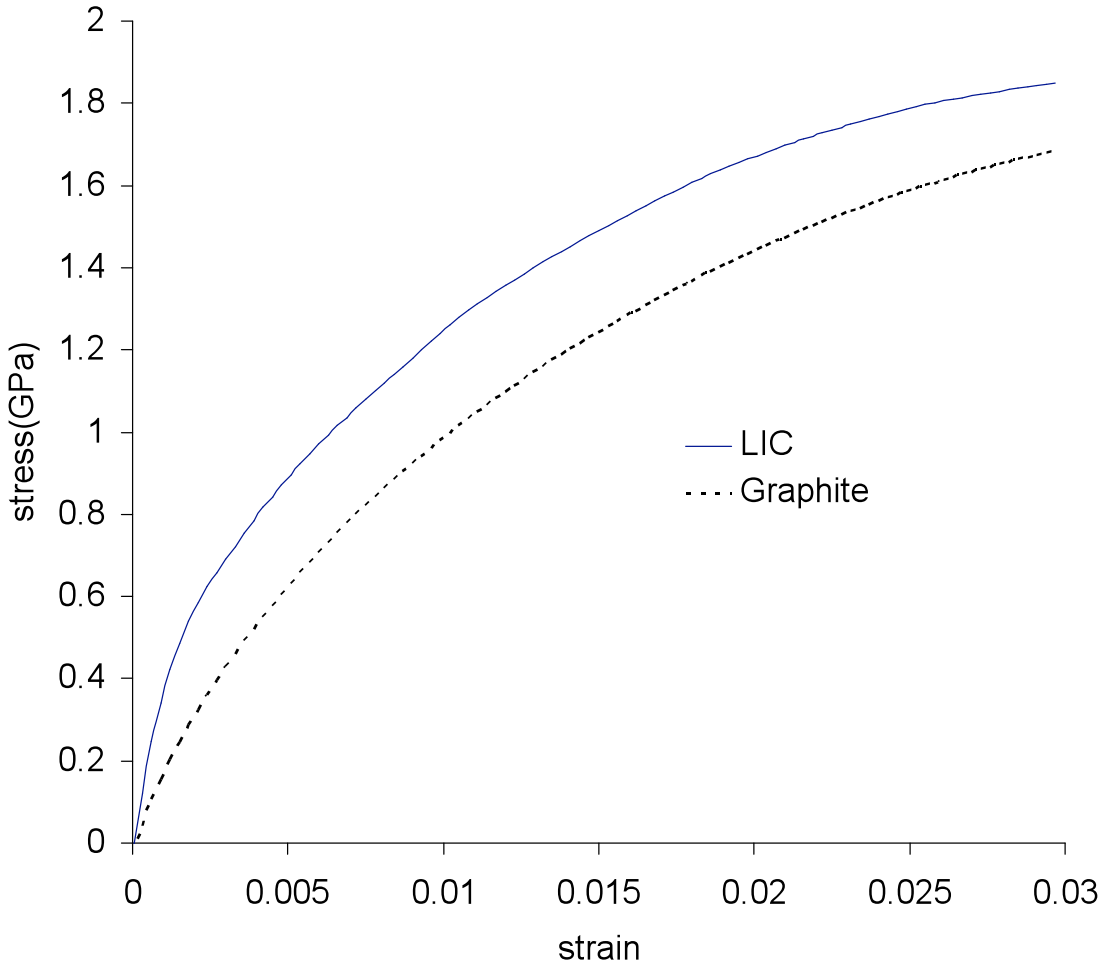

Figure 4.5: stress-strain curve of graphite stretched in perpendicular direction to the graphene lattice

BIBLIOGRAPHY

48. Lehnert, W. and Schmickler, W., 1992, "The diffusion of lithium through graphite: a Monte Carlo simulation based on electronic structure calculations," Chemical Physics, v.163, pp.331-337.

49. Shimizu, A. and Tachikawa, H., 2001, "The dynamics on migrations of Li+ Ion and Li atom at 700 K around the circumference of graphite cluster model: A direct molecular dynamics study," Chimcal Physics Letters, v.339, pp.110-116.

50. Marquez, A. and Balbuena, P.B., 2001, "Molecular Dynamics Study of Graphite/Electrolyte Interfaces," Journal of the Electrochemical Society, v.148, pp.A624-A635.

51. Yao, Z.H., Zhu, C.C., Cheng, M., and Liu, J.H., 2001, "Mechanical properties of carbon nanotube by molecular dynamics simulation," Computational Materials Science, v.22, pp.180-184.

52. Xiao, J.R., Gama, B. A., and Gillespie, J.W., 2005, "An analytical molecular structural mechanics model for the mechanical properties of carbon nanotubes," International Journal of Solids and Structures, v.42, pp.3075-3092.

53. Agrawa, P.M., Sudalayandi, B.S., Raff, L.M., and Komanduri, R., 2008, "Molecular dyanamics (MD) simulations of the dependence of C-C bond length and bond angles on the tnensile strain in single-wall carbon nanotubes (SWCNT)," Computational Materials Science, v.41, pp.450-456.

54. Liew, K.M., Wong, C.H., and Tan, M.J., 2006, "Tensile and compressive properties of carbon nanotube bundles," Acta Materialia, v.54, pp.225-231.

55. Yakobson, B.I., Campbell, M.P., Brabec, C.J., and BErnholc, J., 1997, "High strain rate fracture and C-chain unraveling in carbon nanotubes," Computational Materials Science, v.8, pp.341-348.

56. Meo, M. and Rossi, M., 2006, "Tensile failure prediction of single wall carbon nanotube," Engineering Fracture Mechanics, v.73, pp.2589-2599.

57. Brenner, D.W., 1990, "Empirical potential for hydrocarbons for use In simulating the chemical vapor deposition of diamond films," Physical Review B, v.42, pp.9458-9471.

58. Song, M.K., Hong, S.D., and No, K.T., 2001, "The Structure of Lithium Intercalated Graphite Using an Effective Atomic Charge of Lithium," Journal of the Electrochemical Society, v.148, pp.A1159-A1163.

59. Tachikawa, H., and Shimizu, A., 2005, "Diffusion dynamics of the Li+ ion on a model surface of amorphous carbon: A direct molecular orbital dynamics study," Journal of Physical Chemistry B, v.109, pp.13255-13262.

60. Uchida, T., Morikawa, Y., Ikuta, H., and Wakihara, M., 1996, "Chemical Diffusion Coefficient of Lithium in Carbon Fiber," Journal of the Electrochemical Society, v.143, pp.2606-2610.

61. Skundin, A.M., Grigoreva, O.Y., Kulova, T.L., and Pouchko, S.V., 2003, "The lithium intercalation into graphite from electrolyte and from solid lithium," Journal of Solid State Electrochemistry, v.8, pp.11-14.

62. Hahn, M., Buqa, H., Ruch, P.W., Goers, D., Spahr, M.E., Ufheil, J., Novak, P., and Kotz, R., 2008, "A Dilatometric Study of Lithium Intercalation into Powder-Type Graphite Electrodes," Electrochemical and Solid-State Letters, v.11, pp.A151-A154.

CHAPTER V

CONCLUSIONS AND FUTURE WORK

Effects of mechanical stresses on lithium ion battery were studied using experiments and computer simulations. In the 2nd chapter about structural analysis of battery, it was intended to identify and quantify various sources of mechanical stresses that may exist in battery applications. Focus was made on structural batteries since this new applications aim to utilize batteries as structural members in devices, but the assessment of structural loadings exerted on batteries and the consequence has not been reported. It was found that stresses due to compressive process during fabrication can be as large as 2000 MPa, possible to break materials and stresses from external loadings were the smallest having less than 1 MPa. As to reasons why the structural loadings affect so little, it is possible that the structural battery examples considered in this study are not intended to be used in severe environments. However, loadings from thermal stress can be as high as 100 MPa since embedding batteries in structure played as confinement hindering thermal expansion.

A battery using carbon fiber was fabricated to directly evaluate the effects of mechanical stresses on battery performance. Diffusion coefficients of lithium ions in carbon fibers were measured while tension tests were applied to the battery. At the same time, loadings supported by carbon fibers were measured while electrochemical cycling was performed. Statistically meaningful relation was not observed for diffusion coefficients depending on different stresses, but force applied to carbon fiber changed

significantly during charging/discharging of batteries, and the magnitude of change in force was strongly correlated with the amount of charges.

Molecular dynamics simulations were performed to examine findings from Chapter 3. Diffusion coefficients of lithium ions were measured while graphite lattices were stressed. Differently from experimental results, significant change in diffusivities was observed. The stiffness in perpendicular direction to graphite lattice also showed change from pure graphite to lithium intercalated one. The sign of change in stiffness was opposite to findings from experiments, clarifying the load variation observed in experiments was caused by other factors.

In summary, structural loadings in a structural battery are not critically detrimental, but caution should be made because the effects may vary depending on applications. A special attention should be paid since loadings a structural battery bears can substantially vary during operation. The perturbation of loads in a structural battery may not be caused by change in stiffness or spacing between graphite lattices, but more likely change in stacking sequence of graphite layers. Further study using X-ray diffraction method may be used to verify the relation between the degree of lattice stacking sequence and the amount of lithium ions intercalated into graphite, or more directly an experimental method can be devised to find how much elongation the change in stacking sequence causes.